SELECTIVE OXIDATION AND REACTIVE WETTING OF AN FE-0.15C-5.5MN-1.17SI-1AL ADVANCED HIGH STRENGTH STEELS DURING CONTINUOUS GALVANIZING

SELECTIVE OXIDATION AND REACTIVE WETTING OF AN FE-0.15C-5.5MN-1.17SI-1AL ADVANCED HIGH STRENGTH STEELS DURING CONTINUOUS GALVANIZING

A Thesis

Submitted to the School of Graduate Studies

in Partial Fulfilment of the Requirements

for the Degree

Master of Applied Science

McMaster University

McMaster University   MASTER OF APPLIED SCIENCE (2021)

Hamilton, Ontario   (Materials Science & Engineering)

TITLE: SELECTIVE OXIDATION AND REACTIVE WETTING OF FE-0.15C-5.5MN-1.17SI-1AL ADVANCED HIGH STRENGTH STEELS DURING CONTINOUS GALVANIZING

AUTHOR: Saba Gol, B.Sc. (Sharif University)

SUPERVISOR: Dr. Joseph R. McDermid

NUMBER OF PAGES: 85

Abstract

Third-generation advanced high-strength steels (3G AHSS) are being developed to assist in vehicle light weighting so that fuel efficiency may be improved without sacrificing passenger safety. 3G-AHSS have received significant interest from the automotive industry as a critical candidate for their unique combination of high strength and ductility. However, due to selective oxidation of the principal alloying elements such as Mn, Si, Al, and Cr at the steel surface during the annealing stage prior to immersion in the galvanizing Zn(Al, Fe) bath, the process of continuous hot-dip galvanizing of these steel is challenging. This thesis determined the influence of annealing process parameters such as oxygen partial pressure and annealing time, on the selective oxidation and reactive wetting of an Fe-0.15C-5.56Mn-1.17Si-1Al (wt%) prototype 3G AHSS during intercritical annealing as well as continuous galvanizing.

Simulated annealing and galvanizing were conducted on the prototype Fe-0.15C-5.56Mn-0117Si-1Al (wt%) 3G steel; Intercritical annealing heat treatments were carried out at 690˚C in a N_2-5 vol pct H_2 process atmosphere under dew points of 223 K (–50 °C), 243 (–30 °C) and 268 K (–5 °C). MnO was the major oxide formed at the outmost layer of the external oxides on all annealed samples. The experimental parameters, on the other hand, had a substantial impact on the morphology, distribution, thickness, and surface oxide coverage.

The greatest Mn surface concentration as well as maximum surface oxide coverage and thickness was obtained by annealing the panels under the 223 K (–50 °C)

and 243 (–30 °C) dp process atmospheres. The oxides formed under these process atmospheres largely comprised coarse, compact, and continuous film nodules. In contrast, MnO nodules formed under the 268 K (–5 °C) dewpoint process, exhibited wider spacing between finer and thinner nodules, which was consistent with the internal oxidation mode, while under 223 K (–50 °C) dp process atmosphere, generally external oxidation took place.

Poor reactive wetting was obtained for the panels annealed under the 223 K (–50 °C) dp process atmosphere for both the 60 s and 120 s holding times as well as the 243 K (–30 °C) dp process atmosphere for 120 s. This was attributed to formation of a thick, compact oxide layer on the steel surface, which acted as a barrier between the substrate and Zn bath, preventing Fe dissolution from the substrate surface for the formation of the desired $Fe_2Al_5Zn_x$ interfacial layer. However, a well-developed interfacial Fe-Al intermetallic layer was formed under the 268 K (–5 °C) and 243 (–30 °C) dp process atmospheres for intercritical annealing times of 60 s, which is indicative of a good reactive wetting since the thinner and nodule-like oxides on the steel surface after annealing encourage the reactive wetting. External oxides morphology plays a dominant role in facilitating the contact between Zn-alloy bath and the substrate via different mechanisms such as aluminothermic reduction which occurred for the sample annealed under the 268 K (–5 °C) dp process atmosphere.

Acknowledgments

I would like to thank my supervisor, Dr. Joseph McDermid for his guidance and continuing financial and mental support during my time as a graduate student. I am so grateful to him for providing opportunities to work in a professional and unique group. I had a truly worthwhile experience at CAMC group owing to his encouraging, friendly, and professional attitude. I would also like to thank my supervisory committee members Dr. Joseph Kish for his valuable help.

I would like to thank the International Zinc Association Galvanized Autobody Partnership (IZA-GAP) for their financial support and U.S. Steel Research for providing the substrate material.

I would like to thank John Thomson and Ray Fullerton (McMaster Galvanizing Simulator), Travis Casagrande, Chris Butcher and Jhoynner Martine from the Canadian Centre for Electron Microscopy, Dr. Elizabeth McNally and Dr. Mike Bruhis and Dr. Daniella Pallisco from CAMC who assisted with analysis, training, and support.

Finally, I would like to thank my family for their continued support from miles away and letting me come to Canada although I know how tough it was not seeing their daughter for a few years.

Abbreviations and Symbols

List of Abbreviations

1G	First Generation
2G	Second Generation
3G	Third Generation
AHSS	Advanced High Strength Steels
ART	Austenite Reverse Transformation
BIW	Body In White
CGL	Continuous Galvanizing Line
CP	Complex Phase Steel
DP	Dual Phase Steel
IAT	Intercritical Annealing Temperature
IR	Infrared
M	Martensite
MART	Martensitic Steel
MGS	McMaster Galvanizing Simulator

PHS   Press Hardened Steel

Q&P   Quench and Partition

SEM   Scanning Electron Microscope

TE   Total Elongation

TEM   Transmission Electron Microscope

TM   Tempered Martensite

TRIP   Transformation Induced Plasticity

TWIP   Twinning Induced Plasticity

U.S. DOE   United States Department of Energy

UFG   Ultra Fine-Grained

UTS   Ultimate Tensile Strength

YS   Yield Strength

YPE   Yield Point Elongation

Table of Contents

List of Tables

List of Figures

Chapter 1: Introduction

1.1. Advanced High Strength Steels

Vehicle weight reduction is well accepted as a cost-effective way to minimize carbon dioxide emissions and improve fuel economy. A variety of specialized advanced high strength steels (AHSSs) have grown in popularity over the last two decades and have been widely developed and used in the body in white [1,2]. A new generation of AHSS with the improved combinations of strength and ductility, such as twinning induced plasticity (TWIP) steel, Quench and Partitioning (Q&P) steel, and medium Mn steel, have been successfully used or produced in recent years in response to rising demands by the automotive industry [3,4]. The fraction of AHSS in steel-intensive vehicles can be significant. For example, the 2013 Honda Accord Body-in-White (BIW), shown in Figure 1.1, comprises 51% AHSS [5].

Figure 1.1: The 2013 Honda Accord BIW containing 51% AHSS [5].

Dual phase (DP), transformation-induced plasticity (TRIP), complex phase (CP), martensitic (MART), and press hardened (PHS) steels are among the first generation (1G) AHSS. These grades have a ferritic matrix with different volume fractions of high-strength reinforcing phases, including martensite, bainite, and/or transformable retained austenite in their microstructures. A $UTS \times TE \le 20,000$ MPa% [6,7] characterizes the strength-ductility balance of the 1G AHSS. The second generation (2G) AHSS are designed to build on the strength and ductility balance of the first generation (1G) AHSS. The 2G AHSS grades, such as the twining-induced plasticity (TWIP) steels and lightweight steels with induced plasticity (L-IP) grades, have microstructures consisting of transformable austenitic matrix that is stabilized by high levels of alloying additions. The continuous transformation of austenite by either mechanical twinning or stress/strain-induced ε-martensite formation permits these grades to achieve $60,000 \le UTS \times TE \le 80,000$ MPa% [8].

Due to the need to enhance the mechanical properties of the 1G AHSS, the third generation (3G) AHSS have been proposed due to its less alloy content than the 2G AHSS. The United States Department of Energy (U.S. DOE) defined a target 3G AHSS mechanical property window of $36,000 \le UTS \times TE \le 40,000$ MPa% with specific targets of 1500 MPa $\times$ 25% TE and 1200 MPa $\times$ 30% TE, but Matlock et al. [9,10] have advocated a more modest target envelope of $24,000 \le UTS \times TE \le 40,000$ MPa%. The general property windows for the 1G, 2G, and 3G steels are shown in Figure 1.2, along

with the development vector for 3G TRIP-assisted AHSS from their 1G predecessors and the specific U.S. DOE targets after Shutte et al. [11].
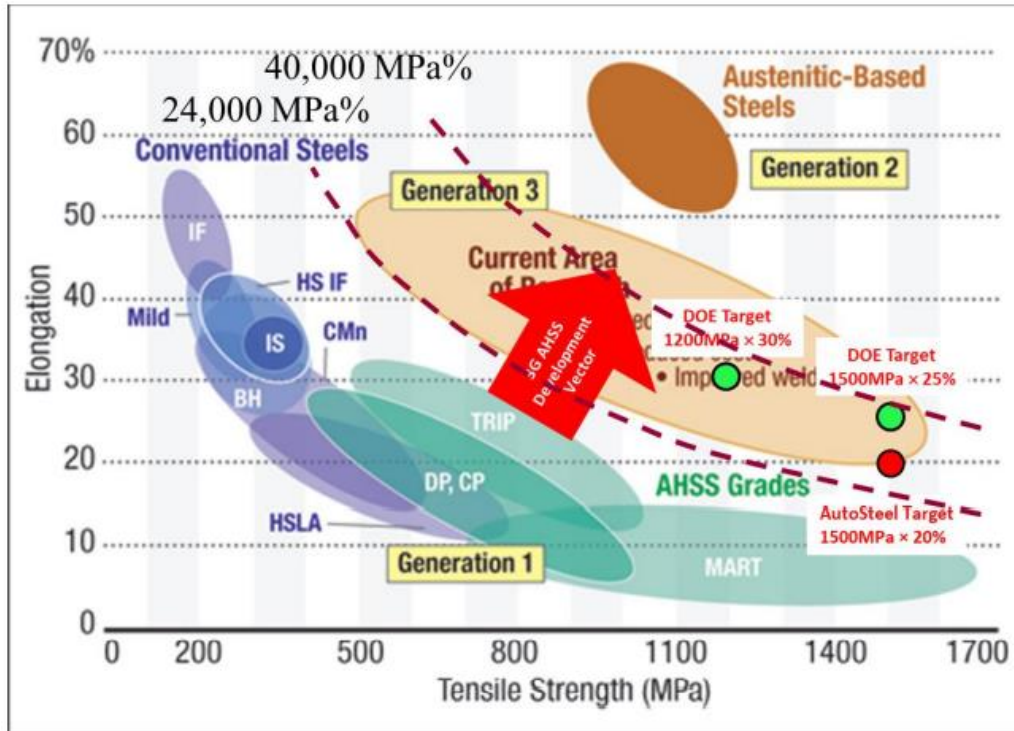
Figure 1.2: General development vector for 3G TRIP-assisted AHSS with general AHSS property window targets and specific U.S. DOE targets for 3G AHSS after Shutte [11].

TRIP-assisted medium-manganese steels are amongst the best candidates of 3G AHSS [11]-[13]. In addition to the alloying additions C, Si, Al, Cr, Ti, Nb, and V, these alloys include 5% to 10% Mn. These steels depend on the maximum quantity of retained austenite, chemically stable, and the mechanical activation mechanisms for improving plasticity such as TRIP and TWIP [14][15]. Several researchers have shown that retained austenite's volume fraction and stability is dependent on both the initial microstructure and thermal processing cycles [16].

However, automotive steels are susceptible to corrosion when exposed to the environment while in service. There have been sufficient scientific studies on corrosion protection [17]. Research results show that the use of an appropriate barrier on its surface can mitigate steel corrosion and thus can delay the ambient effect on steel corrosion. Zinc is commonly and extensively used as a material for steel. Zinc coatings offer not only a steel barrier protection shield but also sacrificial protection. The most economical industrial process for robust corrosion safety for steel substrates is continuous galvanizing. Thus, thermal processing cycles designed to achieve the mechanical property objectives must be compliant with the current processing capability of the continuous galvanizing line (CGL) [18]. Many experiments have been able to obtain excellent strength and ductility balances, which fall within the 3G AHSS mechanical property envelope; however, the intercritical annealing temperature holding times tended to be very long, making the thermal cycles incompatible with the CGL [19].

The objective of this research will focus on identifying potential CGL-compatible candidate processing routes for a prototype medium-Mn TRIP-assisted steels Fe-0.15C-5.5Mn-1.17Si-1Al with the overall objective of achieving 3G AHSS target mechanical properties while allowing reactive wetting of the substrate by conventional CGL Zn(Al, Fe) galvanizing (GI) baths.

Chapter 2: Literature Review

2.1. Third Generation Advanced High-Strength Steels

Medium-Mn high strength steels are amongst the most promising and novel automotive steel solutions for improving the car body light-weighting and safety. The compatibility of medium-Mn TRIP-assisted steels' processing routes with the continuous galvanizing line, which provides a cost-effective means of corrosion protection required for their application in the automotive industry, is of particular interest [2]. To be effectively integrated into vehicle designs, these steels must be protected from corrosion, and the continuous galvanizing process is a cost-effective way to do so. However, the processing routes for 3G AHSS must be chosen to optimize the mechanical properties of the alloys without jeopardizing the substrate galvanizability [20].

In Chapter 1, the different generations of advanced high strength steel (AHSS) were addressed. The first generation (1G) AHSS have a lean alloy composition and the strength and ductility balance of 1G-AHSS ranging within the UTS $\times$ TE $\leq$ 20,000 MPa% range [1,2,3]. The strength and ductility balance of 2G-AHSS is within the range of 60,000 MPa% $\leq$ UTS $\times$ TE $\leq$ 80,000 MPa%, and they have higher levels of alloying additions. Matlock et al. [9] suggested a strength and ductility balance for 3G-AHSSs mechanical property range of 24,000$\leq$ UTS $\times$ TE $\leq$ 40,000 MPa%.

Complex Phase (CP) and TRansformation Induced Plasticity (TRIP) steels are two AHSS grades that are currently being used or are being investigated by steel manufacturers, in addition to DP steels. "First generation" AHSS refers to these three steel grades. The "second generation" AHSS includes steels with twining induced plasticity (TWIP), lightweight steels with induced plasticity (L-IP), and shear band reinforced steels (SIP). Figure 2.1 [21]-[23] shows a summary of representative tensile properties compared to conventional steel grades. The most commonly used AHSS grades are the DP and MART steels. Improved strength and formability, good weldability, relative ease of production, and availability are all reasons for interest in DP steels [24].
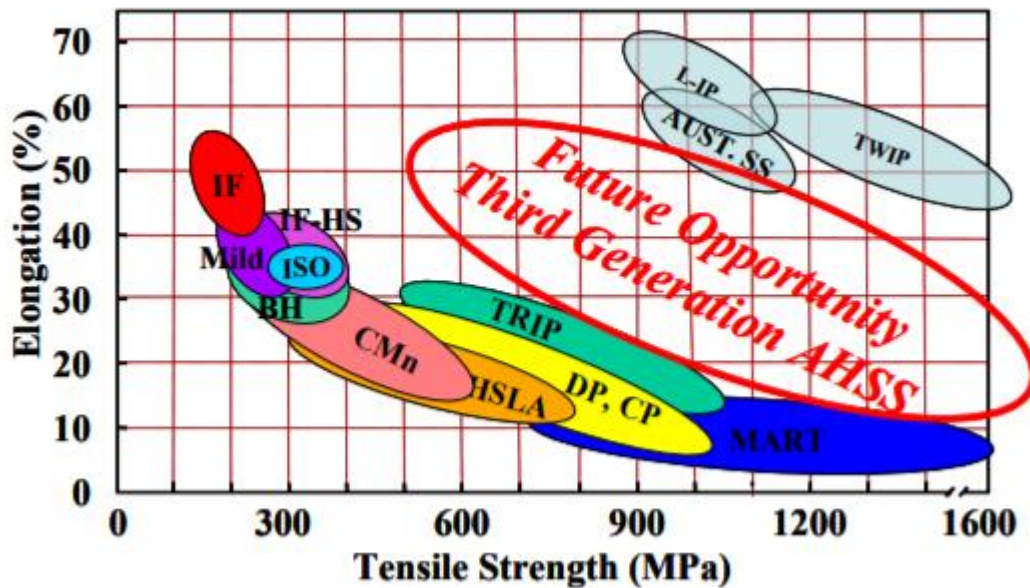
Figure 2.1: Overview of tensile strength and total elongation combinations for different classes of conventional and advanced high strength sheet steel (AHSS) grades [21].

TRIP steel grades show improved strength/elongation combinations due to the strain-induced transformation of retained austenite into martensite, which results in increased strain hardening. Although the mechanical properties of the second generation AHSS steels are obviously superior, the cost of producing these austenitic grades increased significantly due to the high amount of alloying additions. Furthermore, the industrial processing of these alloys, especially TWIP steels with high manganese contents, has proven to be extremely difficult, and TWIP grades have shown to be susceptible to delayed hydrogen cracking [25].

Figure 2.1 shows that there is a property gap between the existing AHSS available. First and second generation grades and defines the future AHSS "Third Generation" property band. Therefore, the recent research has concentrated on filling this property window with modified or new processing routes in which industrial feasibility and cost-effectiveness should naturally also be given special attention.

A system design methodology to determine specific combinations of microstructural constituents leading to properties in the opportunity band is needed for potential production of 3G-AHSS, which is shown in Figure 2.2. Design considerations for AHSS third generation were recently debated using a simplified composite model [3],[27],[28]. Examples were martensite/ferrite and microstructures of martensite/transformable austenite. The calculation results achieved by varying the relative phase fractures in hypothetical microstructures are illustrated in Figure 2.2 with the data points that correspond to the fixed relative phase fractions overlapping the

property combinations. The predicted tensile characteristics for the hypothetical ferrite/martensite microstructures overlap clearly with the characteristics of the 1G-AHSS. The property band for the transformable austenite/martensite mixtures is located within the desired "third-generation" regime between the AHSS bands of the first and second generation [29].

The transformation of metastable austenite with strain was included in a subsequent phase of the modeling effort [30]. As shown in Figure 2.2 (a), four hypothetical austenite stability conditions were considered. Figure 2.2 (b) shows the strength/elongation combination estimates as a result of the different austenite stability. The individual data points on each curve correspond to different initial austenite contents (assumed to range from 0 to 85 percent), with the remainder of the microstructure being ferrite, as indicated by letters A through D.

The predicted properties are clearly influenced by austenite stability. The condition with the least stability (condition D) results in martensite formation at low strains and properties that correlate with the 1G-AHSS band, suggesting that austenite does not make a significant contribution to improved properties.
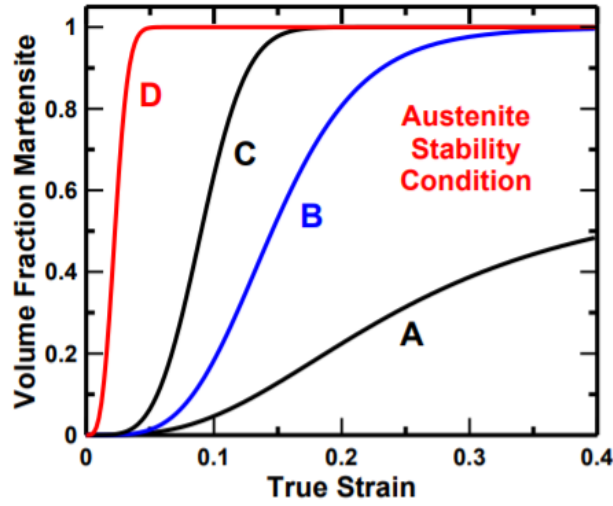
(a)
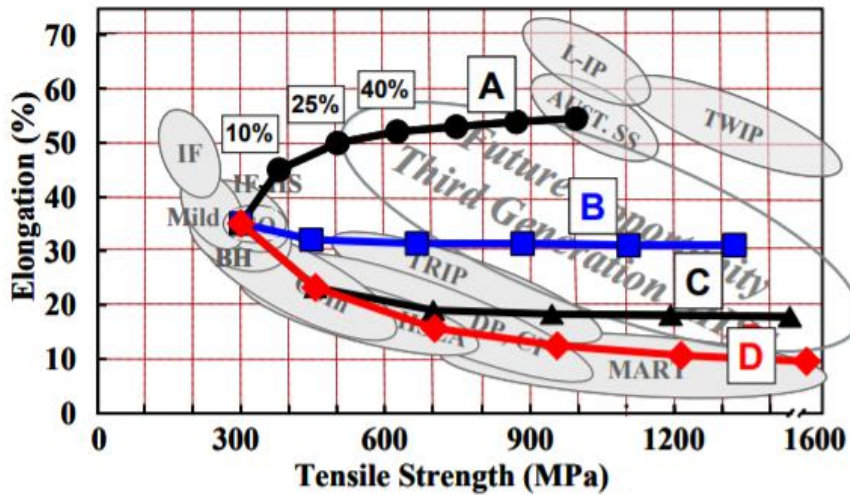
(b)

Figure 2.2: (a) Effect of austenite stability on predicted mechanical property combinations for (a) four different austenite stabilities identified as A through D [29]. (b) predicted mechanical property combinations corresponding to ferrite plus austenite with the different austenite stabilities shown in (a). In (b) each data point on each curve corresponds to an initial austenite fraction, ranging from 0 to 85% [29].

Large volume fractions of relatively stable austenite are expected to have the strongest combination of strength and ductility (curve A in Figure 2.2 (b)). This model was built with simplified assumptions, and more work is being done to build more refined models [30]. However, this fairly straightforward approach provides an understanding of the contribution of the individual constituents and suggests that, in order to obtain the next generation of AHSS steels, complex microstructures consisting of significant fractions of high strength phases, which may be martensite, bainite, or ultrafine-grained ferrite, in combination with highly ductile austenite with controlled stability against the transformation of austenite to martensite with strain.

The aim of ongoing AHSS research is to improve strength and/or ductility beyond what is currently available in the 1G-AHSS without substantially enriching alloy additions or with the goal of lowering the alloying compositions versus the 2G-AHSS. A summary of some of the methods being followed has been given and briefly discussed. The following are some of these strategies: implementation of new processing routes including quenching and portioning (Q&D), modification to traditional TRIP steel processing, development of high strength steels with ultrafine bainitic microstructures, and processing to enhance the properties of DP steels [31],[32].

2.1.1. Enhanced DP Steels

Increasing the martensite volume fraction by altering the carbon content and/or intercritical annealing temperature will easily increase the strength of Dual Phase steels. DP780, DP980 and DP1180 were produced in this manner and are now commercially

available. Microstructural refinement as a result of special hot deformation trials has led to strength increases; the Deformation Induced Ferrite Transformation (DIFT) is one of them [33].

2.1.2. Ultrafine Bainite

The formation of ultrafine bainitic microstructure has recently been studied [34-36]. Theoretical simulations have shown that alloys that can be processed at low temperatures, resulting in intriguing strength-ductility combinations. As an example, low transformation temperatures of 125-325 °C, for example, were used in a study of a 0.98C-1.89Mn-1.46Si-1.26Cr-0.2Mo-0.09V (wt. pct) alloy that led to hardness of 600HV and a ultimate tensile strength of 2.5 GPa. The microstructure was produced after 15-day heat treatment, which may be too time-consuming for industrial applications. Therefore, further experiments have been done on growing bainite kinetics, decreasing heat treatment to hours rather than days by adding alloying additions such as Al and/ or Co [37-39].

2.1.3. Modified TRIP Steels

TRIP steel study began with grades with higher carbon contents than are commonly found in commercially available grades. Matsumura et al. studied 0.4CMnSi grades [40,41], and it was shown that the high carbon content leads to properties that are worth considering in the sense of 3G-AHSS steels. Microalloying has also been used to optimize the grain refinement of TRIP steels. It was suggested that tensile strength levels up to 1 GPa and ductility levels of nearly 20% total elongation have been achieved.

2.1.4. Quenching and Partitioning

Quenching and Partitioning (Q&P) has been recently regarded as a potential method of manufacturing martensitic steels with higher levels of retained austenite. This method consists of a two-step heat treatment in which steels quenched to a quench temperature (QT) in the M_s and M_f temperature range is used to develop a partially martensitic, partially austenitic microstructure. The next stage, known as partitioning, intends to carbon enrich austenite through (partial) carbon depletion of martensite and carbon transfer to austenite. As a result, after final processing (quenching), carbon stabilized austenite is preserved in the microstructure. It is worth mentioning that partitioning can be done at a higher temperature than the QT referred to as two-step Q&P or at the quench temperature, which is known as one-step Q&P. Adding molybdenum impedes bainite transformation kinetics and has also been proven that increases the retained austenite volume fraction, while replacing silicon with aluminum has been shown to speed up the bainite reaction and decreases the retained austenite volume fraction. High retained austenite fractions are assumed to increase strength and ductility if it is chemically stable [42]-[44].

2.2. Medium Manganese Third Generation Advanced High Strength Steels TRIP Steels

Grange and Miller [45,46] proposed medium manganese TRIP-assisted steels, which are candidates to achieve 3G-AHSS properties. 5Mn-7Mn and 0.11C were the first alloy compositions suggested by Miller [47] demonstrated that by annealing a cold-

worked sample in the intercritical zone, an ultrafine-grained (UFG) microstructure could be gained. The microstructure is made up of ferrite and austenite. Samples, where austenite converted to martensite as specimens were deformed, had the best combination of strength and tensile elongations.

Merwin [48]-[50] suggested an alternative processing concept based on earlier work by Miller [47] to manufacture fine-grained or ultrafine-grained duplex ferrite-austenite microstructures with "medium" manganese (5-7 wt pct) and low carbon (0.1 wt pct) compositions. Recently, manganese enrichment of austenite during intercritical annealing was used to create a variety of microstructures with varying austenite fraction and stability in cold rolled 0.1C, 7.1Mn (wt pct) steel [48]. Steel samples were annealed for 168 hours at temperatures ranging from 575 to 675 °C based on equilibrium thermodynamic calculations [2]. In order to allow Mn partitioning, long annealing times were used. Between 2 and 43 percent retained austenite in a fine-grained ferrite matrix was found in the microstructures. The tensile properties of steel at environmental temperature varied with annealing temperature, as shown in Figure 2.3 (a).

Figure 2.3 (b) compares the strain-induced austenite transformation kinetics to the observed tensile work hardening behaviour as determined by in situ neutron diffraction. There is a clear link between the strain dependence of the work hardening rate and austenite transformation behaviour patterns, where regions of high work hardening are associated with significant austenite transformation. At strains greater than about 0.1, the sample annealed at 600 °C showed significant austenite transformation, with martensite formation effectively delaying necking and increasing elongation. Figure 2.3 shows the

influence of austenite stability on tensile properties, which confirms the previously

mentioned trends in Figure 2.2. [29].
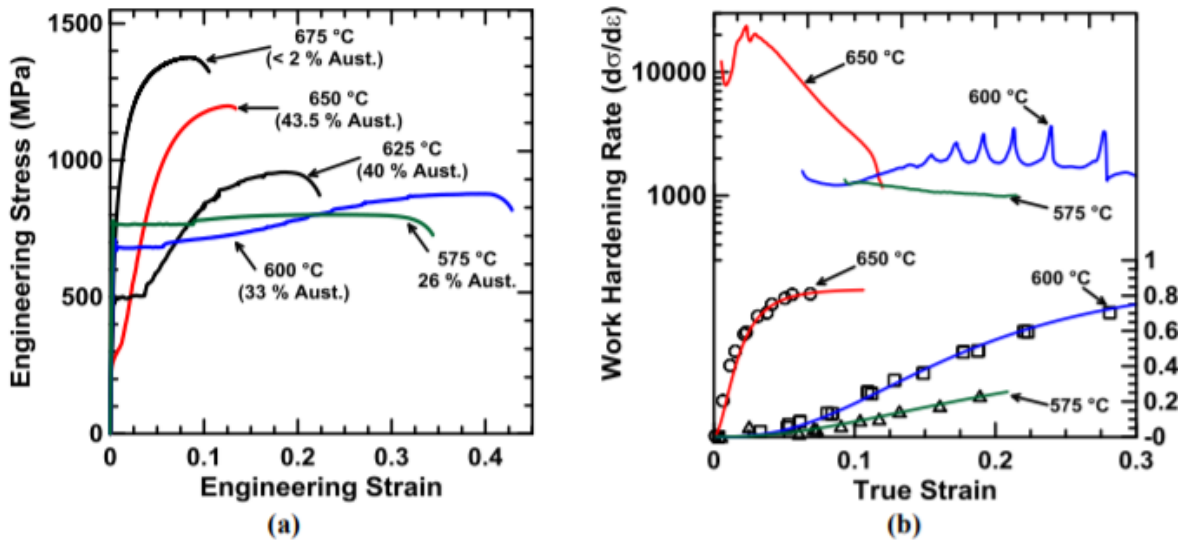
Figure 2.3: (a) Engineering stress-strain curves for a 0.1C, 7.1 Mn (wt pct) steel annealed for one week at indicated temperatures, and (b) fraction of austenite (initial fractions shown in Figure 2.3 (a) transformed with strain as observed with in-situ neutron diffraction experiments on samples along with the strain dependence of the work hardening rate [53].

Medium Mn TRIP steels have an alloy composition of 0.05 wt.% to 0.4 wt.% C; 4

wt.% to 12 wt.% Mn; 0.5 wt.% to 3 wt.% Al; 0.5 wt.% to 2 wt.% Si and trace amounts of

microalloying elements such as Ti, Mo, and V [51,52]. Manganese and carbon are the

best austenite stabilizers that increase the alloy's hardenability. The chemical stability of

retained austenite is dictated by C partitioning during intercritical annealing, which has a

significant impact on mechanical properties. Si and Al, on the other hand, are ferrite

stabilizers that raise the transition temperatures (Ac_1 and Ac_3 temperatures). This requires

higher intercritical temperatures (IATs), which increases alloying element diffusion

kinetics. The formation of chemically stable retained austenite in the as-annealed

microstructure allows for shorter IAT holding times [53] due to faster partitioning of C and Mn to intercritical austenite. Carbides have low Si and Al solubilities. As a result, Si and Al are excellent carbide nucleation barriers. Preventing carbide formation improves the chemical stability of retained austenite by increasing the partitioning of C and Mn to the intercritical austenite. High-Al alloys can lead to an as-annealed microstructure of delta ferrite [54].

The volume fraction of retained austenite and its chemical stability has been shown to be dependent on the starting microstructure, IAT, and IAT holding times [15],[55]. The mechanical properties were determined by the stability of the retained austenite, which was achieved through the activation of one or more plasticity enhancing mechanisms during deformation [56]. Greater mechanical properties are critical for vehicle weight reduction, but the alloy must be able to be galvanized, which is usually achieved through the continuous hot-dip galvanizing process, to be industrially feasible. McDermid and Pourmajidian [57] and Pallisco [58] successfully galvanized a 0.1C-6Mn-2Si alloy and 6Mn-1Si alloy, respectively.

2.3. Chemistry of Medium-Mn TRIP-Assisted Steels

The chemical and mechanical stabilization of large volume fractions of retained austenite at room temperature, as well as the suppression of carbide formation during cooling, are critical to the mechanical properties of medium-Mn TRIP-assisted steels. Since Ni is expensive and Cu is known to cause problems with hot-shortness, austenite stabilizers such as C and Mn are chosen for alloying. Due to their low solubility in

cementite, the ferrite stabilizers Si and Al are also considered for their ability to delay carbide formation. While Si is a strong solid solution strengthener, its selective oxidation in the CGL environment has attracted attention in replacing it with Al, which will oxidize internally in the CGL environment [58]. Cr and Mo are carbide formers that have been applied to TRIP-assisted steels with a medium Mn content to increase hardenability. As grain refiners and precipitation hardeners, Ti, Nb, and V are promising candidates for micro-alloying [60]-[62].

It is also essential to understand the effects of alloying additions on transformation temperatures. Lowering the M_s temperature, which is accomplished by alloying with C, Mn, Si, Cr, Mo, Ni, and/or Nb, will increase the stabilization of retained austenite. The addition of Si, Al, and P would raise the Ac_1 and Ac_3, potentially allowing for improved austenite reversion kinetics due to the increased intercritical annealing temperature [63]. Significant amounts of Al, on the other hand, can result in final microstructures containing either ferrite or delta ferrite [64].

2.4. Strengthen Mechanisms of Transformation-Induced Plasticity Steels

The sustained instantaneous high work hardening rates obtained during plastic deformation are largely responsible for TRIP-assisted steels' high strength and ductility. At high strains, the incremental work hardening exponent, n_{incr} (defined by Equation 2.1 used for TRIP steels [65]), remains high, delaying the onset of necking, which occurs when n_{incr} equals the true stress calculated using the Consider criterion (Equation 2.2) [66]. Since the transformation kinetics for all their investigated alloys and heat treatments

followed a clear relationship with the normalized flow stress, McDermid et al. [67] showed that stress could be used to construct a unified model of the transformation rather than the complicated strain models.

$$n_{incr} = \frac{d(ln\sigma)}{d(ln\varepsilon)} \qquad (2.1)$$

$$\sigma = \frac{d\sigma}{d\varepsilon} \qquad (2.2)$$

In a study of low-alloyed TRIP-assisted steels, Jacques et al. [68] suggested that the shape switch and volumetric expansion that follow the phase transformation produce dislocations in the surrounding ferrite in addition to the dislocations that are caused by normal strain hardening. The TRIP effect, according to Perlade et al. [69], strengthens austenite by partitioning austenite grains and lowering the dislocation mean free path. However, as the TRIP effect reduces the amount of retained austenite during deformation, the strengthening of austenite is probably a less significant factor. Moreover, the yield strengths of ferrite, bainitic ferrite, austenite, and martensite with neutron diffraction were evaluated by Jacques et al. [68], using a mixture law but excluding martensite to model the global stress of low-alloy TRIP assisted steel. There was a clear difference in calculated and experimental stresses, and it was suggested that it should correspond with the martensite reinforcement, which constantly developed during the deformation.

It is obvious that the stability of retained austenite is essential in maintaining high work hardening rates during the deformation period since retained austenite is gradually

transformed to martensite for optimal mechanical properties. In TRIP-assisted steels, two retained austenite morphologies can be found: lamellar (which has an elongated morphology or blocky (more equiaxed morphology). Lamellar retained austenite, due to the increased carbon content and the mechanical stabilizing effects of the surrounding phases, has been shown to be more stable than the blocky retained austenite. Lamellar retained austenite, due to the increased carbon content and the mechanical stabilizing effects of the surrounding phases, has been shown to be more stable than blocky retained austenite [69]-[72].

2.5. Austenite Reversion Kinetics

Intercritical annealing of Medium-Mn steels from the fully martensitic microstructures or cold rolled result in austenite reverse transformation (ART). The formation of austenite from tempered martensite (TM) or martensitic (M) starting microstructures has been widely studied in order to determine the conditions necessary to obtain sufficient amounts (0.35 volume fraction) of retained austenite in the final microstructure that are chemically stable and gradually transform to martensite with deformation which leads to high strength and ductility. Austenite nucleates at martensite lath boundaries, martensite block boundaries, and previous austenite grain boundaries during ART annealing, leading in a UFG microstructure of ferrite, martensite, and retained austenite [73]. The chemical and mechanical stability of retained austenite is improved by the UFG size and partitioning of C and Mn [74].

As-annealed samples' microstructural development as well as mechanical characteristics are influenced by the initial microstructure. Arlazarov et al. [75] investigated the intercritical annealing of a 0.1C-4.6Mn alloy from the TM and M starting microstructures. As-annealed microstructures from the M starting microstructure had both globular and lamellar properties, whereas those from the TM starting microstructure had a globular morphology. Figure (2.4) depicts a schematic of microstructural evolution which was provided by Arlazarov et al.
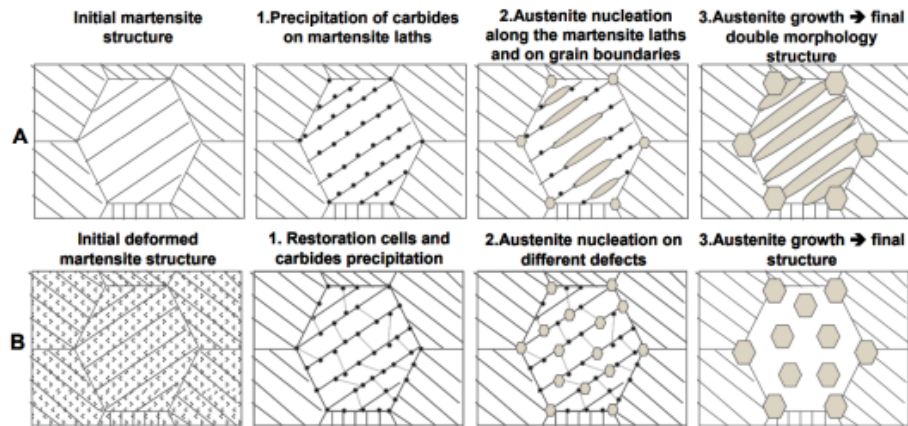
Figure 3.4: Microstructural evolution from the (a) M starting microstructure and (b) TM starting microstructure [75].

Prior to the precipitation of carbides at high angle grain boundaries such as prior austenite grain boundaries, which became nucleation sites for austenite, partial recrystallization took place from the TM starting microstructure, known as the deformed martensite structure, resulting in a homogeneous distribution of austenite and a globular morphology of the as-annealed microstructure (Figure 2.4(B)). Carbides precipitated along martensite lath boundaries (low angle boundaries) as well as high angle grain

boundaries from the M starting microstructure, producing a lamellar and globular morphology of the as-annealed microstructure (Figure 2.4(A)).

The microstructural evolution and mechanical properties of medium-Mn TRIP-assisted steels are strongly influenced by the starting microstructure, according to recent pieces of literature [76,77]. Several researchers have found that a martensitic starting structure results in higher volume fractions of retained austenite than a cold-rolled or cold-rolled and tempered martensitic microstructure. The austenite reversion kinetics of a heat-treated 0.1C5Mn (wt %) steel were investigated by Nakada et al. [76], who found accelerated kinetics in samples with a martensitic starting structure due to C supersaturation, resulting in samples with greater volume fractions of stable retained austenite. They also discovered that the austenite grains and the martensite matrix had a Kurdjumov-Sachs (K-S) orientation relationship and that there was an Mn concentration gradient within the martensite matrix, implying that Mn diffusion into austenite dominated austenite growth (Figure 2.5). The partitioning local equilibrium model is dominant in the martensite to austenite transition and is driven by Mn diffusion, according to an additional analysis by these authors using DICTRA 14 simulations. The high density of austenite nucleation sites inthe martensite lath system and the comparatively faster Mn diffusion in the martensite matrix is thus due to the faster austenite reversion kinetics [77].
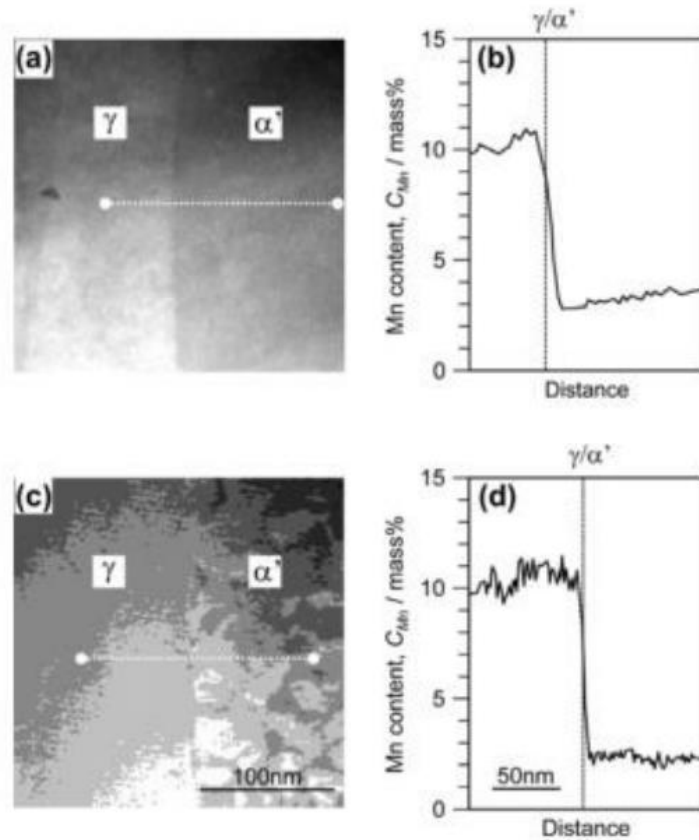
Figure 2.5: STEM image and Mn concentration profile across the austenite/martensite interface in 0.15C-5Mn (wt%) steel annealed at 636°Cfor (a, b) 1000 s and (c, d) 50 hrs [76].

2.6. Mechanical Properties of Medium-Mn TRIP-Assisted Steels

Several authors have found yield point elongation and serrated flow in medium-Mn TRIP-assisted steels, despite the fact that they can achieve excellent strength and ductility.

Gibbs [77] noticed a systemic shift in the tensile behavior of 5.1Mn, 5.8Mn, and 7.1Mn steels as the annealing temperature increased. The steels were water quenched after being annealed for 168 hours. All of the steels showed an improvement in work hardening rate and ultimate tensile strength with an increase in intercritical annealing

temperature but a decrease in yield strength and degree of discontinuous yielding. When the annealing temperature of 5.1Mn steel was above 600 °C, and 5.8Mn and 7.1Mn of steels over 650°C, the yield point elongation vanished completely. Serrated flow and strain localization were observed in the samples annealed at 625 °C, especially in the 5.8Mn and 7.1Mn alloys. Gibbs et al. [77] suggested that the reduction in austenite stability with increasing annealing temperature was responsible for improvements in mechanical properties, but they did not go into detail about yield point elongation or serrated flow.

Sun et al. [78] studied a 0.2C-10.3Mn-2.9Al (wt%) steel that was intercritically annealed at 700°C or 750°C for five minutes and then water quenched to produce a duplex ferrite-retained austenite microstructure. At a macroscopic engineering strain rate of $6{\times}10^{-4}$ Uniaxial tensile tests were conducted. Each sample had a different plastic flow behavior. The sample that was annealed at 750°C had visible serrated flow (beginning after the Lüders strain), while the sample that was annealed at 700°C did not. The 750°C sample was found to have a discontinuous strain-induced martensitic transition within the Portevin-Le Chatelier (PLC) bands, according to the researchers (Figure 2.6). In the study into a cold-rolling, intercritically annealed 0.14C-7Mn-0.23Si steel, Wangs et al. [79] disagreed with this conclusion. A strain-induced martensitic transition occurred in the

Lüders band but was not noticeable in the PLC bands, according to hardness studies,

XRD, and thermal measurements.
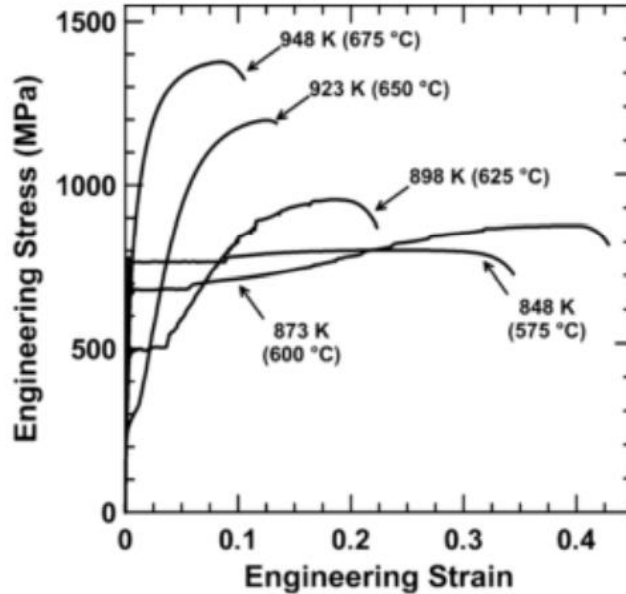
Figure 2.6: Engineering stress-strain curves for 7.1Mn steel annealed for 168 hours and water quenched [77].

2.7. Continuous Hot-Dip Galvanizing

Medium-Mn TRIP-assisted steels must be protected from aqueous corrosion in order to be used in automotive applications, for which the continuous hot-dip galvanizing procedure is a cost-effective solution. Zn-based metallic coatings offer a physical barrier between the ground and the corrosive atmosphere. They also provide galvanic protection by acting as a sacrificial anode if the physical barrier is harmed [80]-[83].

Sendzimir-type continuous galvanizing mechanism is depicted schematically in Figure 2.7 by Silva [80]. The steel coils are first welded together to form a continuous strip before being washed with alkali brushing (using hot 1.5-2.5 percent NaOH(aq)) to

dissolve and remove organics, soils, and fines. Electrolytic cleaning may then be used to strip soils and Fe fines that are more strongly adherent. The strip is then dried after several rinsing stages before entering the annealing furnace, which is usually either a direct-fired furnace, a radiant tube furnace, or a mixture of both technologies. CGLs normally use the N_2-(5-20%) H_2 environment with a regulated oxygen potential in order to reduce any Fe oxides on the steel surfaces to ensure that the Zn bath can react with the metallic Fe. A planar gas jet is used to strip excess coating using air or nitrogen after the strip has been withdrawn from the bath. Galvanized steels may be cooled to solidify the coating when the zinc bath is applied, but galvannealed steels are further treated to produce a layer composed of a collection of Fe-Zn intermetallic materials before the strip is cooled. After leaving the CGL coating portion, the steel will proceed to temper rolling, roller leveling, pre-phosphating, oiling, cutting, and recoiling until they are packed and delivered.
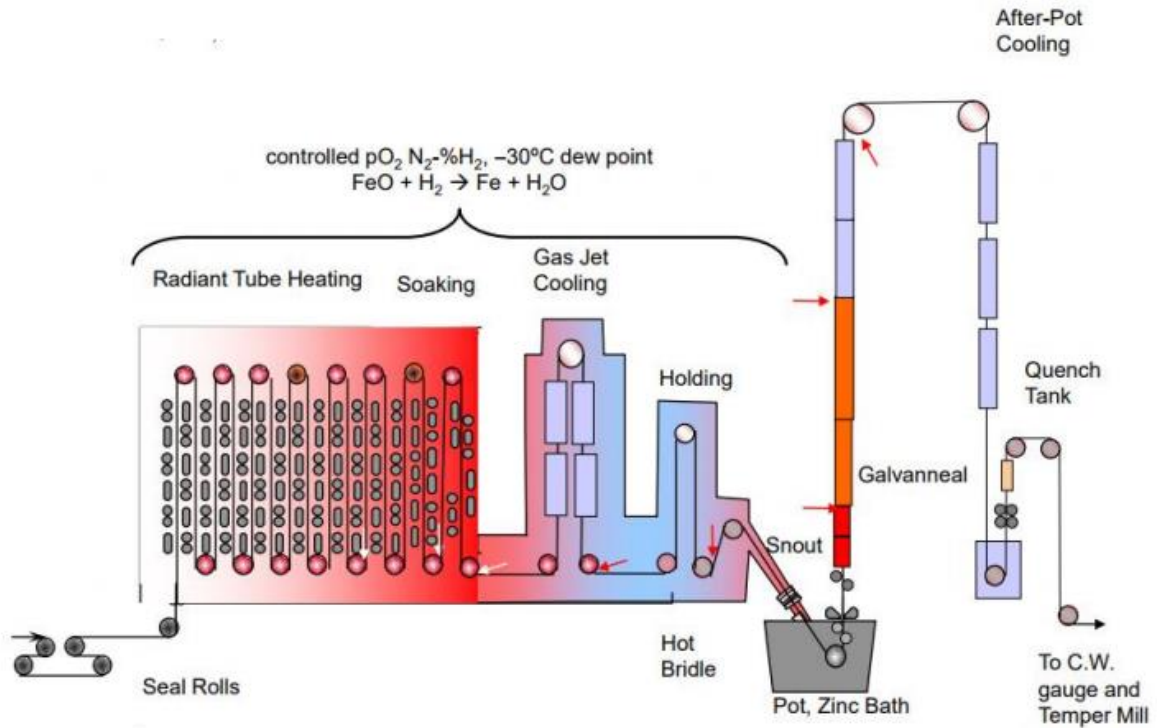
Figure 2.7: Schematic of a continuous hot-dip galvanizing line [80].

2.8. Selective Oxidation

2.8.1 Thermodynamic and theory of external and internal oxidation

The process atmosphere of the CGL consists of a N_2-H_2 combination with a regulated oxygen potential or dew point (T_{dp}). The dew point is known as the temperature at which water vapour condenses for a fixed water vapour partial pressure P_{H2O}, i.e., the temperature at which equilibrium is satisfied in Equation 2.3.

$$H_2O_{(l)} = H_2O_{(g)} \tag{2.3}$$

From the thermodynamic perspective, the simplest oxidation reaction includes and element (M) and oxygen to form the oxide M_xO_y is as follows [84]:

$$xM \text{ (s)}+ y/2O_2 \text{ (g)} \leftrightarrow M_xO_y \text{ (s)} \tag{2.4}$$

The oxygen partial pressure determines the oxide stability, which is calculated from the equilibrium constant for this reaction [84]:

$$log \; k_1 = log \; [(\alpha_M)^x \; (\; p_{O2})^{ \; y/2}] = -\Delta G_1°/(2.303RT) \tag{2.5}$$

Where $\Delta G°$ (J. mol^{-1}) is the Gibbs free energy for the reaction; R is the universal gas constant (J K^{-1} mol^{-1}); and T is the reaction temperature (K). Therefore, according to 2.4), while the prevailing oxygen partial pressure (pO_2) is higher than the pO_2 of (2.4), an oxide is likely to form. In this respect, M_xO_y is presumed to be a pure condensed species ($\alpha_{MxOy} = 1$). Oxygen partial pressure of the annealing atmosphere is controlled by H_2 content and dew point (T_{dp}) of the atmosphere. T_{dp} is defined as a temperature at which reaction (2.3) is in equilibrium.

If $H_2O_{(l)}$ is assumed to be a pure and condensed, the partial pressure of $H_2O_{(g)}$ is driven by:

$$log \; k_3 = log \; [p_{H2O \; (g)}] = -\Delta G_3°/(2.303RT) \tag{2.6}$$

In order to determine the partial pressure of $H_2O_{(g)}$ from Eq. (2.6), the oxygen partial pressure can be calculated from Eq. (2.7) and Eq. (2.8) at the equilibrium condition, in that the H_2 content is constant at the annealing atmosphere:

$$H_{2(g)} + 1/2O_{2(g)} = H_2O_{(g)} \tag{2.7}$$

$$log \; k_5=log \; [pH_2O/pO_2^{0.5} \; pH_2]=-\Delta G_5°/(2.303RT)=(-230000-8.14Tln(T)+9.25T) \; /$$
$$(2.303RT) \tag{2.8}$$

By the combination of Eq. (2.4) and Eq. (2.7), it can be driven that [84]:

$$x/y \; M \; (s) + H_2O \; (g) \leftrightarrow y^{-1}M_xO_y \; (s) + H_2 \tag{2.9}$$
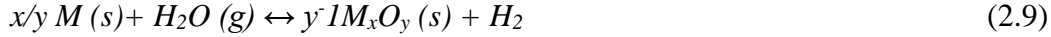
Figure 2.8 shows the critical oxygen potentials as a function of temperature for various alloying elements of relevance to medium-Mn 3G AHSS with the thermodynamic data obtained from [85]. CGL atmospheres typically comprise N2-5%H2 with a -30°C dew point process atmosphere. As can be seen in Figure 2.8, the CGL atmosphere (with a dew point of -30°C or -10°C) is reductive to Fe oxides but oxidizing to Al, Cr, Mn, and Si.
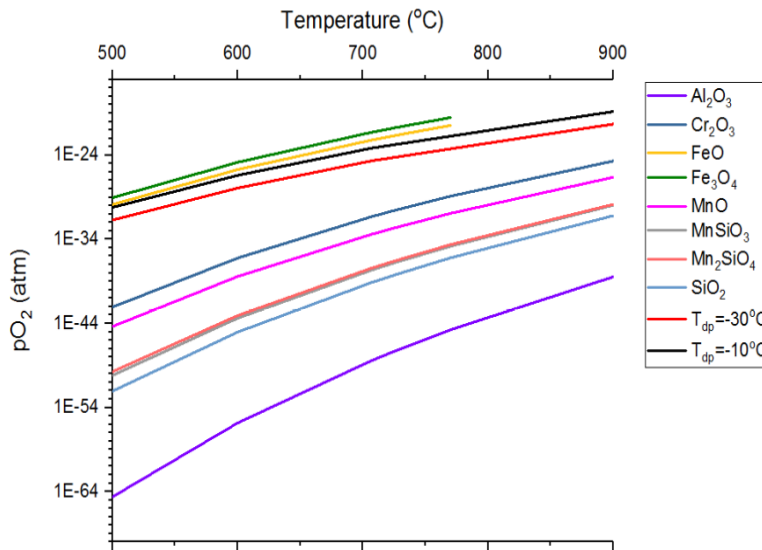
Figure 2.8: Critical oxygen potentials for the oxidation of various metallic elements in a N2-5%H2 atmosphere as a function of annealing temperature, assuming unit activity of the metallic species. Also indicated are the oxygen potentials for a -30°C and -10°C dew point atmosphere [85].

2.8.2. External-Internal transition for the oxidation

Depending on where the oxides form, either on the substrate surface or in the alloy matrix beneath the free surface; two modes of selective oxidation (external and internal oxidation) can be considered [86]. The oxygen partial pressure of annealing atmosphere, temperature, the concentration of alloying elements, etc. are the variables which have significant effects on the oxidation mode [87]. For internal oxidation, various theories have been introduced. The first theory which correlated to the internal oxidation of binary alloy was proposed by Wagner in 1959 [88]. In the original Wagner model, it was assumed that a single oxidizing element forms a single oxide with a zero solubility product in the matrix. Wagner has proposed that the mode of oxidation is dictated by the competition between inward oxygen flux and outward alloying element flux. Internal oxidation happens when flux of oxygen into the substrate is higher than flux of the alloying element towards the steel surface, which extends until an oxide compact layer blocks the oxygen diffusion, where internal to external oxidation transition occurs. Various modifications have been suggested to improve Wagner model in predicting oxidation mode of the elements during heat treatments, which will be discussed in the following sections.

2.8.3. Wagner Model

Wagner came up with a theory for the isothermal transition between internal and external oxidation of single crystal binary *A-B* alloys, where *A* is the matrix and *B* is the alloying element, forming a single oxide BO_v. The transition from external to internal

oxidation happens when the molar concentration of B, $N_B^{(O)}$, is lower than the critical

molar concentration of B, $N_{B\,Critical}^{(O)}$,which is given as below

$$N_B^{(O)} < N_{B\,Critical}^{(O)} = \left[\frac{\prod g*Vm\,N_O^{(S)}\,Do}{2v\,D_B V_{BO}}\right]^{1/2} \tag{2.10}$$

Here, N_O^S is the dissolved oxygen molar concentration at the surface, D_O refers to the

diffusion coefficient of oxygen, D_B indicates the diffusion coefficient of B element, V_m

cites the molar volume of the alloy, V_{BOv} is the oxides molar volume, and g^* mentions to

the critical oxide volume fraction. Wagner has asserted that when g, the oxide volume

fraction, reaches to a critical value (g^*) the inward diffusion path for oxygen will be

blocked and the internal to external oxidation transition happens. Rapp [89] has applied

Wagner model for Ag-In alloys and determined g* as 0.3.

Besides, from Eq. (2.10), It can be concluded that an increase in D_B ; such as a

reduction of the grain sizes, can lead to a reduction in $N_{B\,Critical}^{(O)}$. Also, the solubility and

permeability of oxygen in the substrate as well as change in temperature will have

considerable effects on the external to internal oxidation transition [89].

Although the original Wagner model remains a cornerstone of literature on the

external to internal transition, Wagner assumed severe restrictive hypotheses which limit

the use of original Wagner model. These assumptions especially involve (1) the

consideration of binary alloys, (2) the formation of a single oxide phase with a zero-

solubility product in the matrix, (3) the spherical morphology of the internal oxides, (4)

the oxidation of the only most reactive metal and (5) parabolic growth of the oxide layer.

2.9. The Zn(Al, Fe) Bath

If a pure Zn galvanizing bath was used in the CGL, the series of intermetallics would form and multiple layers of lower Fe content phases such as gamma (Γ-Fe_3Zn_{10}), delta (δ-$FeZn_{10}$), zeta (ζ-$FeZn_{13}$), and eta (η- metallic Zn) move away from the substrate. Since the thermodynamic driving force for Fe-Al intermetallic formation is higher, small additions of Al to the continuous galvanizing baths are used to avoid the formation of these brittle Fe-Zn intermetallic compounds at the steel/coating interface. The Fe-Al interfacial layer ($Fe_2Al_{5-x}Zn_x$) is industrially known as the "inhibition" layer because it serves to prevent or "inhibite" the formation of brittle Fe-Zn t inter-metallic compounds by acting as a barrier to diffusion between Fe and Zn, thus allowing the Zn to remain metallic [90,91].

A Zn-rich corner of the ternary phase Zn-Al-Fe diagram reveals the low solubility of Al and Fe in liquid Zn with a widely used CGL 460°C bath temperature, as seen [92]. The higher Fe metastable solubility close to the steel strip, as seen in Figure 2.9, leads to the persistent dissolution of Fe and the precipitation of dross in the bath [92]. The supersaturation of Fe causes Fe intermetallic compounds to nucleate and precipitate on the steel surface, depending on the bath Al content.
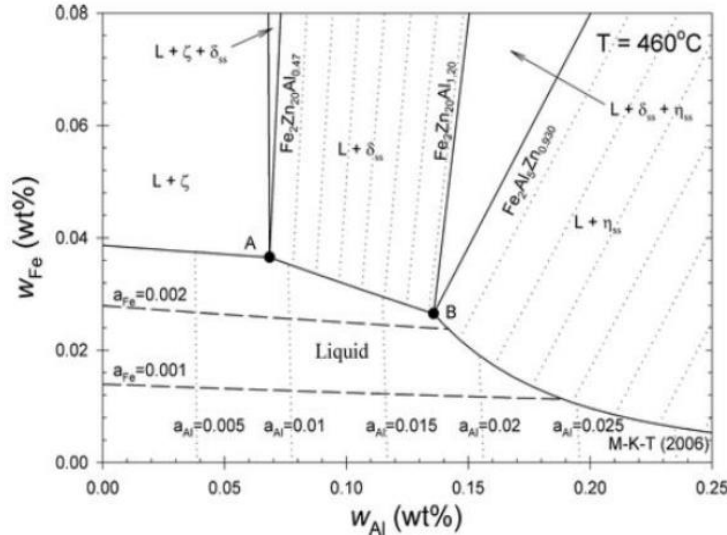
Figure 2.9: Zn-rich corner of the Zn-Al-Fe ternary phase diagram with isoactivity lines for Al (with respect to pure solid Al) and Fe (with respect to pure solid α-Fe) in the liquid phase [92].

Chen et al. [93] explored the creation of interstitial layers on an interstitial-free (IF) steel galvanized in a traditional 0.2wt% dissolved Al bath. As the steel is immersed in the liquid Zn, the metastable equilibrium between the Zn(Al, Fe) bath and Fe causes Fe dissolution from the steel strip, resulting in supersaturation of the liquid Zn bath by Fe, as seen in Figure 2.10. To restore thermodynamic equilibrium to the system configuration, this local Fe supersaturation is one of the drivers for the nucleation and growth of a compact layer of fine crystals of the metastable $FeAl_3$ phase or stable $Fe_2Al_{5-x}Zn_x$ phase at the substrate/bath interface. The formation of this layer prevents further Fe dissolution into the bath, but the diffusion of Fe through the layer will continue, as will the diffusion of Zn and Al towards the substrate. The transformation of $FeAl_3$ to $Fe_2Al_{5-x}Zn_x$ will take place as described in Equation with an upper, coarse layer of $Fe_2Al_{5-x}Zn_x$ formation. The final interfacial layer will have a two-layer composition due to the continued transition $FeAl_3$ of to $Fe_2Al_{5-x}Zn_x$: an outer layer of coarser and arbitrarily aligned $Fe_2Al_{5-x}Zn_x$

crystals on top of a finer, compact, preferentially oriented $Fe_2Al_{5-x}Zn_x$ layer according to Equation 2.11.

$$FeAl_3 + 2Al_{(bath)} + Fe_{(substrate)} + Zn_{(bath)} \rightarrow Fe_2Al_{5-x}Zn_x \qquad (2.11)$$
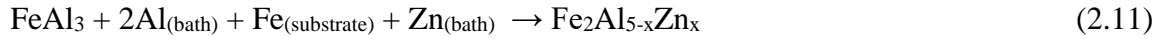
Figure 2.11 illustrates the formation mechanism. The microstructure will consist of a discontinuous sub-layer for baths with low dissolved Al, accelerating interfacial layer degradation and Fe-Zn development of intermetallic phases [94].
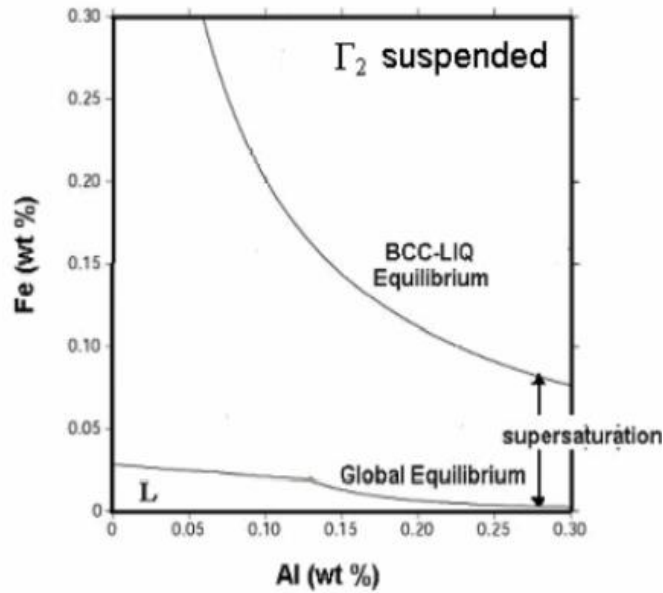
Figure 2.10: Metastble versus equilibrium configuration for the Zn-rich corner of the Zn-AlFe ternary system at 450°C [93].
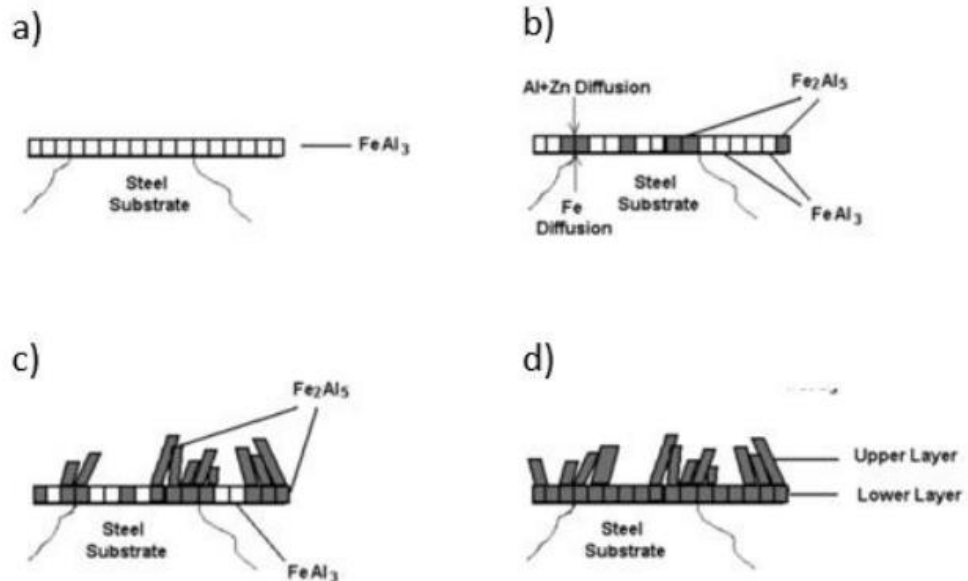
Figure 2.11: The formation of the interfacial layer on an IF steel galvanized in a 0.2wt% [94].

2.10. Strategies to Improve Reactive Wetting of Medium-Mn TRIP-Assisted Steels

According to Liu et al. [95] and Suzuki et al. [96] who calculated ΔG their calculations for the potential aluminothermic reduction reactions of simple oxides in their research by increasing the dew point to between -86 °C and -55°C, mostly Mn_2SiO_4 will form. Dew points above -55°C may result in the formation of MnO and Mn_2SiO_4, while dew points below -70°C should result in SiO_2 formation, which is detrimental to reactive wetting if it is in a film-like morphology at the surface. Despite the fact that the ΔG values they tabulated, as seen in Table2.1, are not sufficiently scaled for relative comparison, they are all very negative, implying that the bath Al could reduce all of the mentioned oxides. Khondker et al. [97] and Bellhouse et al. [98] had previously suggested this finding, at least for MnO, to better understand the high degree of reactive wetting found for their MnO-covered DP and TRIP-assisted steel surfaces, respectively. Despite a coating of MnO on the surface prior to annealing, Liu et al. [95] discovered the $Fe_2Al_{5-x}Zn_x$ layer, which coincided with the mechanism of aluminothermic reduction proposed by Khondker et al. [97] and Bellhouse et al. [98]. Later, Kavitha and McDermid verified the mechanism and found that the kinetics of aluminothermic Mn oxide reduction is linear with time [57].

Table 2.1: Calculated ΔG of possible aluminothermic reduction reactions of simple oxides for a 0.090C-1.43Mn-0.26Si-0.20Cr steel at 460°C [95].

Equation	ΔG (kJ)
$2Al + 3MnO \rightarrow 3Mn + Al_2O_3$	-452.951
$2Al + Cr_2O_3 \rightarrow 2Cr + Al_2O_3$	-506.579
$4Al + 3SiO_2 \rightarrow 3Si + 2Al_2O_3$	-279.346
$2Al + 3P_2O_5 \rightarrow 6P + 5Al_2O_3$	-753.196
$2Al + Fe_2O_3 \rightarrow 2Fe + Al_2O_3$	-819.397

Suzuki et al. [96] during recrystallization annealing at 850°C for 60 seconds in a N_2-3% H_2 atmosphere with dew points varying from -50 to 0°C to predict the selective oxidation behavior of Si, Mn-added AHSS. They developed a thermodynamic model to predict the oxide species that would form during the annealing process as a function of the alloy Si/Mn ratio, assuming local equilibrium at the steel surface, and then tested it with their alloys and data from the literature. Though their thermal cycles did not follow that of conventional TRIP-assisted steel, a comparison can still be made between their experimental results and their thermodynamic model.

Suzuki et al. [96] summarized the oxide species that produced under "low" oxygen potentials (log(pO2) < 21, resulting in selective external oxidation) and "high" oxygen potentials (log(pO2) ≥19, adequate for internal oxidation) based on the literature and their own experimental findings.

Liu et al. [95] built on the concept of a critical Si/Mn ratio for better reactive wetting and added the idea of a critical Al/Mn ratio to prevent Mn_2SiO_4 formation by using ThermoCalc to quantify the conditions under which complex oxides of Mn, Si, and Al can form. They suggested that since the mass ratio of Al to Mn in $MnAl_2O_4$ is around0.98, Mn in excess of this ratio would be free to form Mn_2SiO_4 after consuming the available Al to form $MnAl_2O_4$, while excess Al in the substrate would result in the formation of Al_2O_3. They found that lowering Si and increasing Al to achieve an Al/Mn ratio of 1.25 enhanced the reactive wetting behavior of the base alloy by avoiding $MnAl_2O_4$ on the surface. These models provide useful information about the species that are likely to form during annealing. However, these models cannot predict reaction kinetics, oxide thickness, or morphology, which are essential factors that determine reactive wetting behavior. For example, several researchers have shown that complete surface coverage of the substrate with film-like oxides results in bad reactive wetting [99] but that strong reactive wetting will occur if the oxide nodules are widely scattered because $Fe_2Al_{5-x}Zn_x$ can form between the oxides [100].

Chapter 3: Experimental Methods

3.1. Experimental Steel Fabrication and Composition

The chemical composition of the steel substrate (designated "steel D") used in this investigation, is given in Table 3.1, as determined using inductively coupled plasma mass spectroscopy for all elements except C, which was determined via combustion analysis. The experimental alloy was manufactured at U.S. Steel R & D (Muhall, Pennsylvania) via vacuum melting, slab casting, hot rolling, pickling, trimming, and cold rolling to 1.2 mm thickness. The experimental alloy was cast, heated to 1250°C, and hot rolled to 25mm with a final temperature of 1050°C and then slowly cooled in vermiculite. The ingots were then reheated to 1250°C before being hot rolled to a thickness of 4 mm at 900°C. The hot rolled structure was used to machine dilatometry samples (2mm × 10 mm). The steel was annealed at 665°C for 2 hours and ground to a thickness of 2.7 mm before being cold rolled to a thickness of 1.2 mm.

The samples in the current research were taken from Patel's research [101] which focussed on the microstructural development and mechanical properties of the prototype Fe-0.15C-5.56Mn-1.17Si-0.99Al. samples in this research had as-received microstructure contained approximately 70% tempered martensite, carbides, and ferrite. X-ray diffraction showed that there are no statistically significant amounts of retained austenite in the as-received condition. The annealing temperature was carried out at 690°C at which the best mechanical properties (UTS and TE of 1150 MPa and 0.29 engineering

strain respectively, very close to the specific targets set by the U.S. DOE of UTS and TE of 1200 MPa and 0.30 engineering) were obtained by Petal's research. The as-received microstructure can be seen in Figure 3.1 [101].
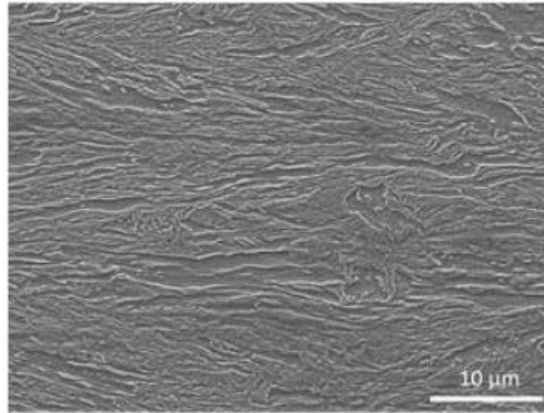
Figure 4.1: SEM image of tempered martensitic (TM) starting microstructure [101].

Table 3.1. Chemical composition of experimental alloy.

C	Mn	Al	Si	S	Mo	Ti
0.15	5.56	0.99	1.17	0.003	0.073	0.011

3.2. Selective Oxidation Experiments

All selective oxidation experiments were performed using the McMaster Galvanizing Simulator (MGS) (Iwatani-Surtec), shown in Figure 3.2. From the top of the apparatus down, the MGS consists of an atmosphere controlled column comprising a sample loading/cooling chamber; a quartz lamp infrared (I.R.) furnace, and a high

frequency (H.F.) furnace used for galvannealing, a gas jet wiping system; and a zinc pot. An airlock separates the two upper sections from the gas jet wiping and zinc pot. The annealing atmosphere is controlled by a dew point control system which mixes a water-saturated stream of gas with a dry stream of gas in the appropriate ratio. The gas mixing chamber is not shown where the desired gas composition is achieved by adjusting the fflows of N_2 and H_2 gases. The sample temperature is controlled using a type K (0.5mm, ±32°C) thermocouple welded directly to the sample prior to the start of the experiment.
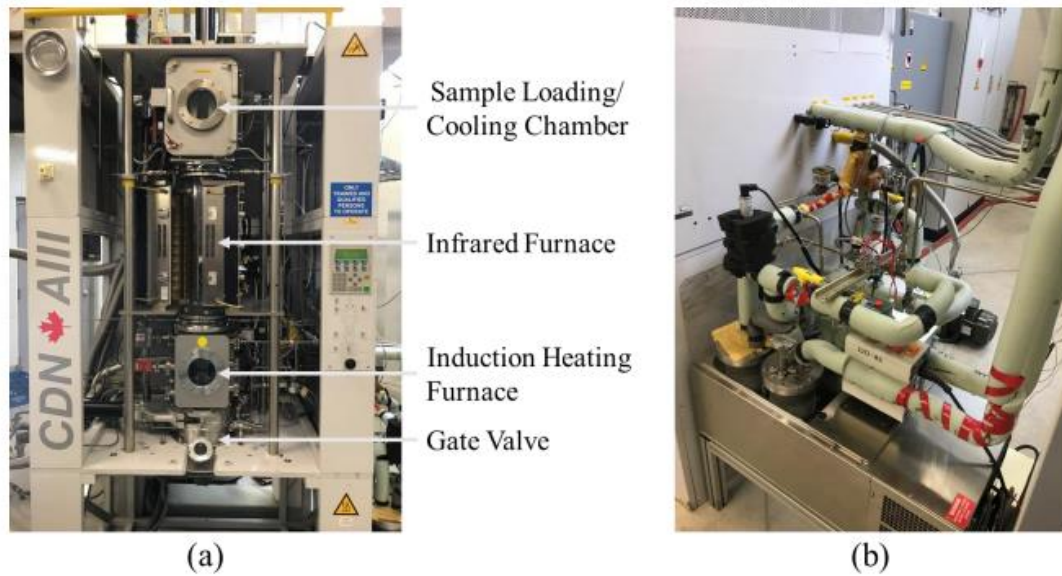
Figure 3.2: (a) McMaster galvanizing simulator (MGS), (b) dew point control system.

Three process atmospheres with dew points of 223 K (–50°C), 243 K (–30°C), and 268 K (–5°C) were selected to explore the effect of oxygen partial pressure on the selective oxidation of Mn and Si. The process atmosphere used in the heat treatments,

including the process atmosphere pO_2 at the 690°C peak temperature for all annealing experiments, is given in Table 3.2.

Table 3.2: Experimental Process Atmosphere at 690°C.

Process Atmosphere dp [K (°C)]	N_2 Content (Vol.%)	H_2 Content (Vol.%)	pH_2O/pH_2	PO_2 (atm)
223(–50)	95	5	0.0010	6.87×10^{-25}
243(–30)	95	5	0.0082	4.39×10^{-23}
258(–5)	95	5	0.0679	3.35×10^{-21}

A schematic thermal profile of the annealing heat treatment employed in this research for Steel D is shown in Figure 3.3. This cycle was developed by Patel [101] based on dilatometry results, austenite reversion kinetics, and the resultant mechanical properties of the substrate while taking into consideration of the constraints of industrial galvanizing lines, including holding time, cooling and heating rates, and limiting temperatures. Samples in this research are as-received sheets which experienced the heat treatment which showed the best mechanical properties based on Patel's thesis [101].

Samples for selective oxidation heat treatments were cut from the parent materials into 10 mm × 50 mm coupons with an abrasive water-jet cutter such that the rolling direction was parallel to the longitudinal axis of the experimental samples.

Prior to the annealing trials, polishing the surface with 4000 grit SiC paper was performed in order to minimize the effects of surface roughness on the selective oxidation

studies. All samples were cleaned in a 2% NaOH solution heated to 80°C to remove surface organics and fines, rinsed with water, ultrasonically cleaned in isopropanol, and dried in a warm air stream. Final cleaning was performed with isopropanol (Fisher Scientific) exactly prior to annealing.

Experimental heat treatments consisted of heating six samples to 500°C at a heating rate of +15°C/s followed by heating to the intercritical annealing temperature (IAT) of 690°C at a heating rate of 5°C/s, holding at the IAT for 60 and 120 s and cooling to 460°C at -10°C/s, holding for 30 s to thermally equilibrate the steel with the galvanizing bath (also at 460°C and cooling at 20°C/s to room temperature. Samples were cooled by N_2 jet cooling. The annealed samples were stored in anhydrous isopropanol (HPLC grade) to minimize further surface oxidation prior to the subsequent tests.
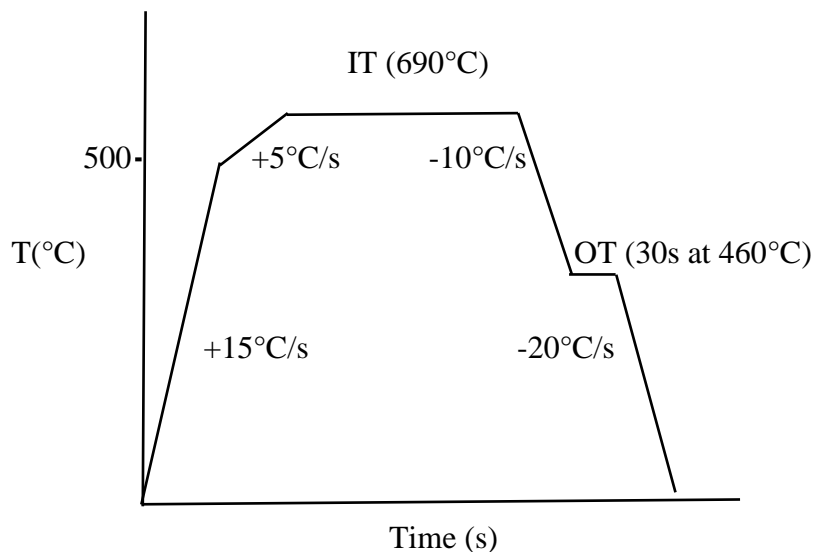
Figure 3.3. Schematic of the experimental thermal cycle.

3.3. Sample Analysis

Scanning electron microscopy (SEM) was performed on JEOL 7000 field emission gun SEM to determine the surface oxide morphology and distribution. The imaging was operated in secondary electron imaging (SEI) mode. An acceleration voltage of 5 keV and a working distance of 6 mm was chosen for all analyses. In order to prevent charging, all oxidized samples were vapour coated with carbon prior to examination.

On the other hand, to examine the growth of oxides on the surface and subsurface, six cross-sectional surfaces were scanned through focused ion beam (FIB) milling to make ten mμ-wide trenches perpendicular to the steel surface. A NVision 40 FIB-SEM microscope was used at an acceleration voltage of 5 keV. Carbon and Tungsten were deposited on the surfaces in order to prevent the surface oxides from damage while the Ga ion beam is milling. Image J 1.48v software was chosen to measure the surface oxide thickness on tilt-corrected SEM images. Because of the large local difference in surface oxide thickness, a minimum of 100 measurements were taken per sample using a grid to ensure that the external oxide layers were randomly collected as Pourmajidian had done in for the first time [15]. A 95% confidence interval was used to record the average oxide thickness for the samples.

X-Ray Photoelectron Spectroscopy (XPS) was used to determine the chemical composition and chemical bonding state of the sample surfaces and subsurfaces as a function of sputtering depth into the sample. In this technique, the specimen is bombarded with X-rays under ultra-high vacuum. The absorption of the X-rays by the

sample results in the ejection of a photoelectron from either a core or valence level electron. The chemical composition and binding energy are obtained by calculating the binding energy of the ejected photoelectron from the measured kinetic energy of the photoelectron according to:

$$E_k = hv - E_B - \varphi_{sp} \tag{3.1}$$

Where E_k is the measured kinetic energy of the photoelectron, h is Plank's constant, v is the frequency of the incident X-rays (making hv the energy of the incident X-ray photons), $E_{B.}$ is the binding energy relative to the Fermi level, and ϕ_{sp} is the work function of the spectrometer (representing the difference between the vacuum and the Fermi level). XPS was performed using a PHI Quantera XPS with an Al Kα X-ray source (1486.7 eV) and 100 μm spot size.

The other test which is required to analyze the fine-scale structure of the surface and subsurface oxides is TEM. Prior to TEM, samples were prepared via Focused ion beam (FIB) milling (NVision 40 by Zeiss). In order to preserve the sample surface during FIB, carbon and tungsten were deposited. An FEI Titan 80-300 TEM microscope equipped with an electron energy loss spectroscopy (EELS) analytical facility was used for TEM analysis. The 60 and 120 s annealing time samples were used preferentially for high-resolution scanning transmission electron microscopy (HR-STEM) and electron energy loss spectroscopy (EELS) analysis. HR-STEM micrographs were acquired using an FEI Titan 80-300HB transmission electron microscope operated at 300 keV. Digital

Micrograph 2.3 software was used to extract elemental maps from the raw EELS data cubes.

3.4. Reactive Wetting Experiments

In order to prepare samples for reactive wetting trials, 120 mm × 200 mm panels were cut from the as-received, 1.2 mm thick cold rolled steel sheet. Prior to dipping, panels were degreased by brushing them in a 353 K (80°C) 2 wt.% NaOH solution. Samples were then rinsed with DI water, followed by a second rinsing step with running DI water, ultrasonically cleaning in isopropanol and ultimately dried in a warm air stream.

Intercritical heat treatment was done at 690°C following the schematic thermal profile documented in Figure 3.1, using (−50°C), (−30°C), and (−5°C) dew point N_2-5vol%H_2 process atmosphere as given in Table 3.2. All of these annealing and galvanizing experiments were carried out in the McMaster Galvanizing Simulator (MGS, Iwatani Surtec). The sample temperature was controlled by a K-type thermocouple.

Experimental heat treatments consisted of heating the samples to 500°C at a heating rate of 15°C/s followed by heating to the intercritical annealing temperature (IAT) of 690°C at a heating rate of 5°C/s, holding at the IAT for 60 and 120 s and cooling to 460°C at 10°C/s, holding for 30 s to the thermally equilibrate the steel with the galvanizing bath, and cooling at 20°C/s to room temperature. Samples were cooled by N_2 jet cooling. Galvanizing experiments include another step before the final cooling comprising dipping the samples for 4 s in a Fe saturated 0.2 wt.% dissolved Al zinc bath

at 460°C [10]. The simulated galvanizing bath comprised 50 kg of melt. The zinc surface

was covered from scratching by wrapping and storing the galvanized panels separately.

Coating property analysis was performed for the 90 mm × 90 mm uniform

temperature and coating area centered in the lower portion of the as-galvanized panels.

Coating adhesion was measured using 90 mm × 10 mm coupons excised from the as-

galvanized plates, according to ASTM A653/A 653M-05 [102]. Based on the galvanized

specimen dimensions (90 mm × 10 mm) and thickness (1.2 mm), a 4.8 mm diameter pin

was used. Inspection of the outer bend surface with a Keyence VHX5000 digital optical

microscopy was used to assess coating adhesion.

The galvanized samples were also subjected to SEM analysis to assess the

interfacial reaction components. The interfacial layer was revealed by two methods of

stripping the zinc overlay: (a) fuming nitric acid (HNO_3) and (b) 10vol% H_2SO_4 in water.

Although stripping with HNO_3 dissolves all but the $Fe_2Al_5Zn_x$ layer, the latter technique

left both the Fe-Zn and Fe-Al intermetallics intact. To prevent charging of the specimen

during SEM examination, the surfaces of all SEM samples were vapor coated with C.

FEI Titan 80-300 transmission electron microscope (TEM) and resident electron

energy loss spectroscopy (EELS) was used to assess the fine-scale cross-sectional

microstructure and chemistry of the oxides produced on the surface and subsurface of the

experimental steel before galvanizing, as well as any reaction products formed at the Fe-

Zn interface after galvanizing. Quantitative point analyses and EELS elemental maps

were both done. TEM samples were prepared using a Zeiss NVision 40 and focused ion

beam (FIB) milling. To protect the sample surface from damage during FIB, carbon and Tungsten were deposited on it. The TEM was set to 300 keV, with an energy resolution of 0.08 eV full-width half-maximum (FWHM) at the zero-loss peak in monochromat

mode. For all samples, Mn-L, O-K, Si-K, Al-L, Zn-L, and Fe-L EELS edges were obtained. Using a Gatan Quantum GIF and Digital Micrograph 2.3 software, elemental maps were extracted from the EELS data cubes during HR-STEM inspection of the selective oxidation and galvanized samples.

Chapter 4: Results

4.1 Selective Oxidation Prediction

Figure 4.1 depicts the expected selective oxidation mode of Mn and Si in ferrite at 963 K (690 °C), in which the transition between external and internal oxidation for Mn and Si has been shown using orange and green lines for both the bulk and along grain boundaries. In Figure 4.1 (a) and (b), the horizontal dashed lines indicate the mole fraction of Mn and Si in the experimental alloy. The predicted oxidation mode for Mn and Si in ferrite and austenite, are summarized in Table 4.1.
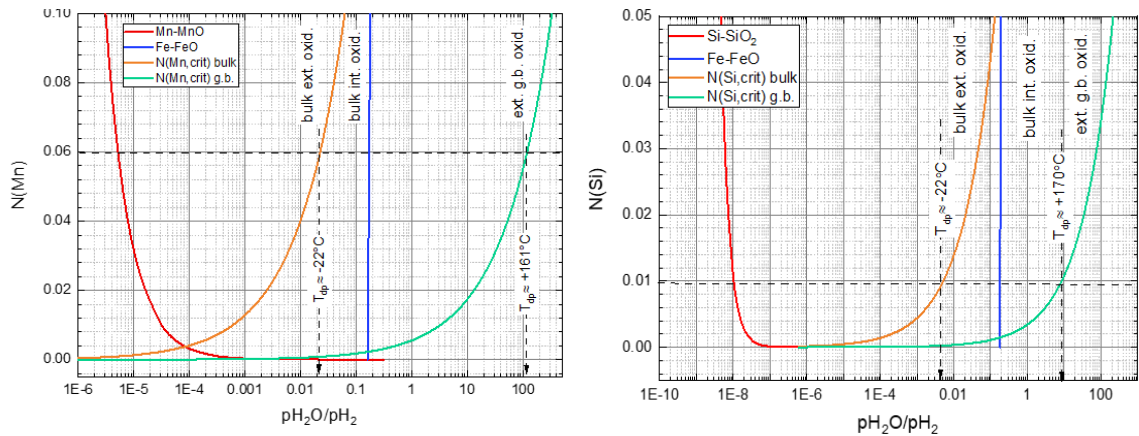
Figure 4.1: Predicted selective oxidation mode of (A) X = Mn and (B) X=Si in a α-Fe-X binary alloy at 690°C in a N$_2$-5 vol.% H$_2$ process atmosphere.

Table 4.1: Predicted Selective Oxidation Mode of Fe-0.1C-5.5Mn-1.1Si at an Intercritical Annealing Temperature of 963 K (690°C) as a Function of Process Atmosphere using the Wagner [103] and Modified Models.

Process Atmosphere Name	Alloying Element	GB Diffusion		Bulk Diffusion	
		Ferrite	Austenite	Ferrite	Austenite
223 K (-50°C) dp	Si	External	External	External	External
	Mn	External	External	External	External
243 K (-30°C) dp	Si	External	External	External	External
	Mn	External	External	External	External
268 k (-5°C) dp	Si	External	External	Internal	Internal
	Mn	External	External	Internal	Internal

4.2. Selective Oxidation

Mn, Al, Si, and some other elements XPS depth profiles are shown in Figure 4.2 to semi-quantitatively determine the surface oxide thickness and the subsurface oxidation mode of alloying elements during annealing under three processes atmosphere. The findings are provided for the most industrially relevant annealing times of 60 s and120 s to compare the effect of time on the selective oxidation of different elements.

Manganese showed significant surface enrichment compared to the bulk concentrations for the lowest pO_2 process atmosphere 223 K (–50 °C)dp, which quickly dropped with increasing depth to values close to the nominal bulk concentration of each element. Increasing the annealing holding time from 60 s to 120 s leads to an increase in

the external oxide layer thickness, which is shown in Figures 4.2 (a) and (b). The restriction of the enrichment zone to the outer surface indicates an external oxidation mode, which is consistent with the Wagner model prediction for manganese (Table 4.1). Therefore, it can be inferred from Figure 4.2 (a,b) that the thickness of the external MnO for both steel samples annealed under the (–50°C) dp process atmosphere increased with increasing annealing time for the mentioned dew point.
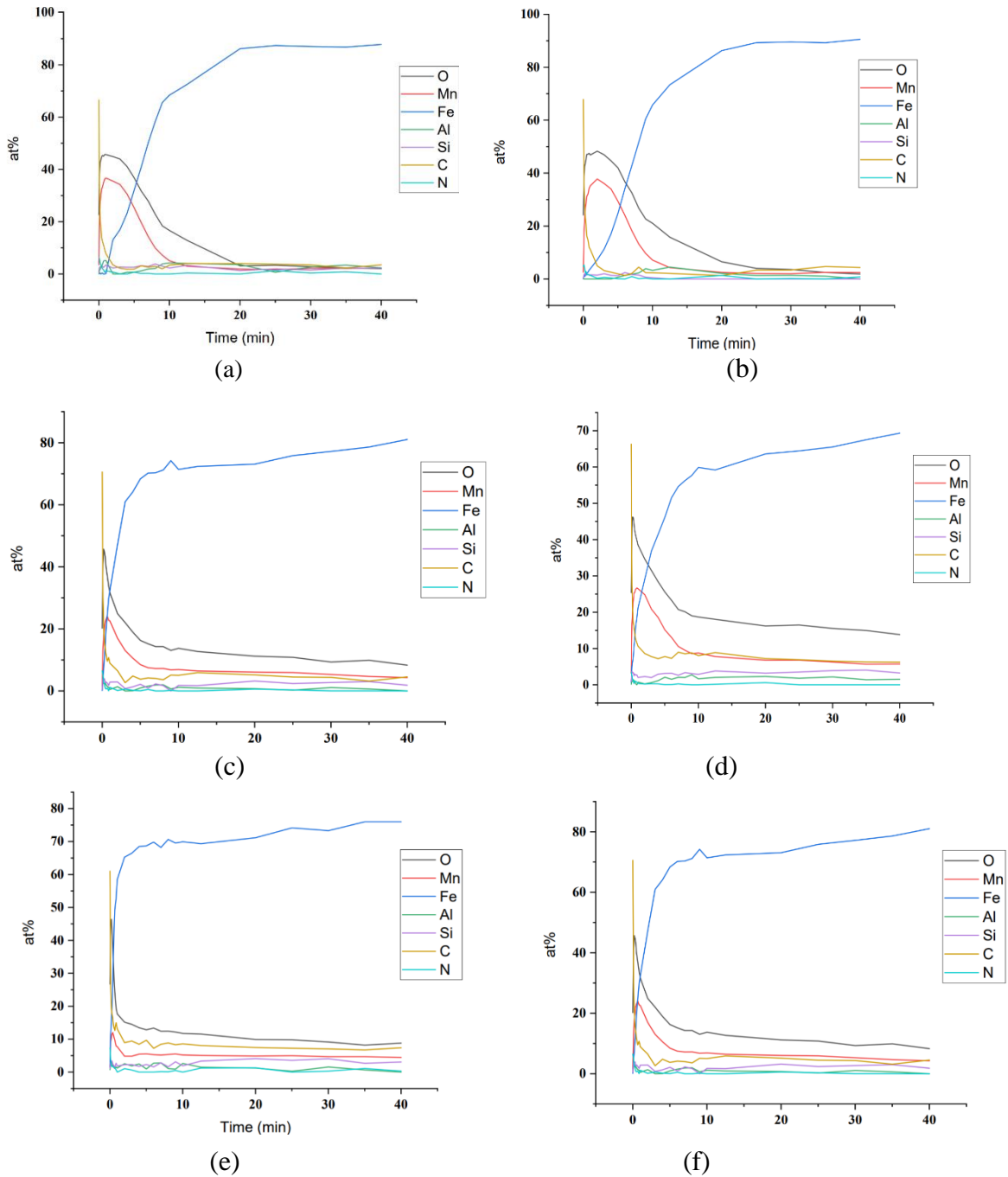
Figure 4.2: Mn, Si and other elemental depth profiles as a function of 690 °C annealing time and process atmosphere pO$_2$: (a) 223 K (–50°C) dp for 60 s, (b) 120 s, (c) 243 K (–30°C) dp for 60 s, (d) 120 s and (e) 268 K (–5°C) dp for 60 s and (f) for 120 s.

Table 4.2: Identification of oxides on the steel surface using XPS.

Process Atmosphere Name	Oxide Phases Present
223 K (–50°C) dp	[$MnSiO_3$, Mn_2SiO_4], MnO, Al_2O_3,SiO_2
243 K (–30°C) dp	MnO, [$MnSiO_3$, Mn_2SiO_4], Al_2O_3,SiO_2
268 K (–5°C) dp	MnO, [$MnSiO_3$, Mn_2SiO_4], Al_2O_3

Increasing the process atmosphere pO_2 to 243 K (–30 °C) dp resulted in enrichment of Mn above the bulk composition deeper into the subsurface, which indicates the transition from the external to internal oxidation had occured. The external oxides for the 243 K (–30 °C) dp process atmosphere samples were substantially thinner than their 223 K (–50 °C) dp process atmosphere counterparts, as shown in Figure 4.2 (c,d). This is indicative that the transition from external to internal oxidation mode has begun. It can also be observed that the depth of internal oxidation rose when the annealing time was increased from 60 s to 120 s as a result of the diffusion-driven process.

Further increasing the process atmosphere pO_2 to 268 K (–5 °C) leads to a significant decrease in external oxide thickness and an increased depth of internal oxidation under the 268 K (–5°C) dp process atmosphere for both annealing times, as can also be seen in Figure 4.2 (e,f). When these data are compared to the Wagner model for 268 K (–5°C) dp process atmosphere (Table 4.1), it is clear that they are strongly correlated for Mn. Consequently, The Wagner and modified Wagner models predicted Mn oxidation mode for ferrite well for all investigated process atmospheres. The Wagner model, on the other hand, anticipated Si external oxidation for the 223 K (–50 °C) dp and

243 K (–30 °C) process environment, which contradicts the XPS findings. However, the Wagner model predicted Si internal oxidation for the 268 K (–5 °C) dp process atmosphere, which is in agreement with the XPS results.

By comparing the obtained XPS binding energies to those found in the literature [107,108], the oxides were identified. The main oxide phases found on steel surfaces are summarized in Table 4.2. For the lower pO_2 223 K (–50 °C) and 243 K (–30 °C), $MnSiO_3$ or Mn_2SiO_4 in addition to MnO and Al_2O_3 were discovered. It should be mentioned that no SiO_2 was identified in the case of the 268 K (–5 °C) dp process atmosphere. $MnSiO_3$ and Mn_2SiO_4 could not be clearly distinguished due to considerable similarities in their Mn $2p_{3/2}$ and O 1s XPS binding energies and are presented by the parentheses in Table 4.2. Therefore, to identify the surface oxides, EELS was used via TEM thin foils.

Figures 4.3 show the morphology and distribution of the external oxides on the experimental steel surfaces intercritically at 963 K (690 °C) for the 223 K (–50°C) dp (Fig. a,b), 243 K (-30°C) dp (Fig. c,d) and 268 K (–5°C) dp (Fig. e,f) process atmosphere where the micrographs at first column represents the external oxides for the samples after 60 s isothermal hold at the IAT and the second column shows 120 s holding time. It is obvious in the figures, that independent of the process atmosphere pO_2, holding the samples at IAT for extended periods resulted in increased surface coverage. Furthermore, the oxide layers produced following the 60 s and 120 s holding times (Figure 4.3 (a) and (b)) are coarser and more compact. This could be anticipated, as extended annealing provided the surface oxides additional time for diffusional growth. For instance, in Figure 4.3 (a) oxide clusters can be observed after an annealing time of 60 s. Figure 4.3 (b)

shows how increasing the annealing period to 120 s caused the oxide clusters to expand and full coverage of the surface by oxides, and no grain boundaries can be seen. This finding is qualitatively consistent with the XPS results (Fig 4.2) showing that extending the annealing period from 60 s to 120 s increases oxide thickness.

At higher pO_2 243 K (–30°C) dp process atmosphere, a decrease in external oxidation was observed compared to 223 K (–50°C) dp process atmosphere. The steel surfaces displayed a thinner external oxide such that some grinding lines are still visible at the surface of the sample annealed for 60 s (Figure 4.3 (c)). Further increasing the annealing holding time resulted in an increase in surface coverage and coarsening of oxides per those observed for the lower pO_2 223 K (–50°C) dp process atmosphere. This finding is consistent with XPS results (Fig 4.2) which showed a reduction in external oxidation and an increase in internal oxidation.

Further increasing the process atmosphere pO_2 using the 268 k (–5°C) dp process atmosphere (Figure 4.3 (e,f)) led to a significant reduction in surface coverage which is in

agreement with the XPS results (Fig 4.2) and the external to internal oxidation transition anticipated by Wagner model [103].
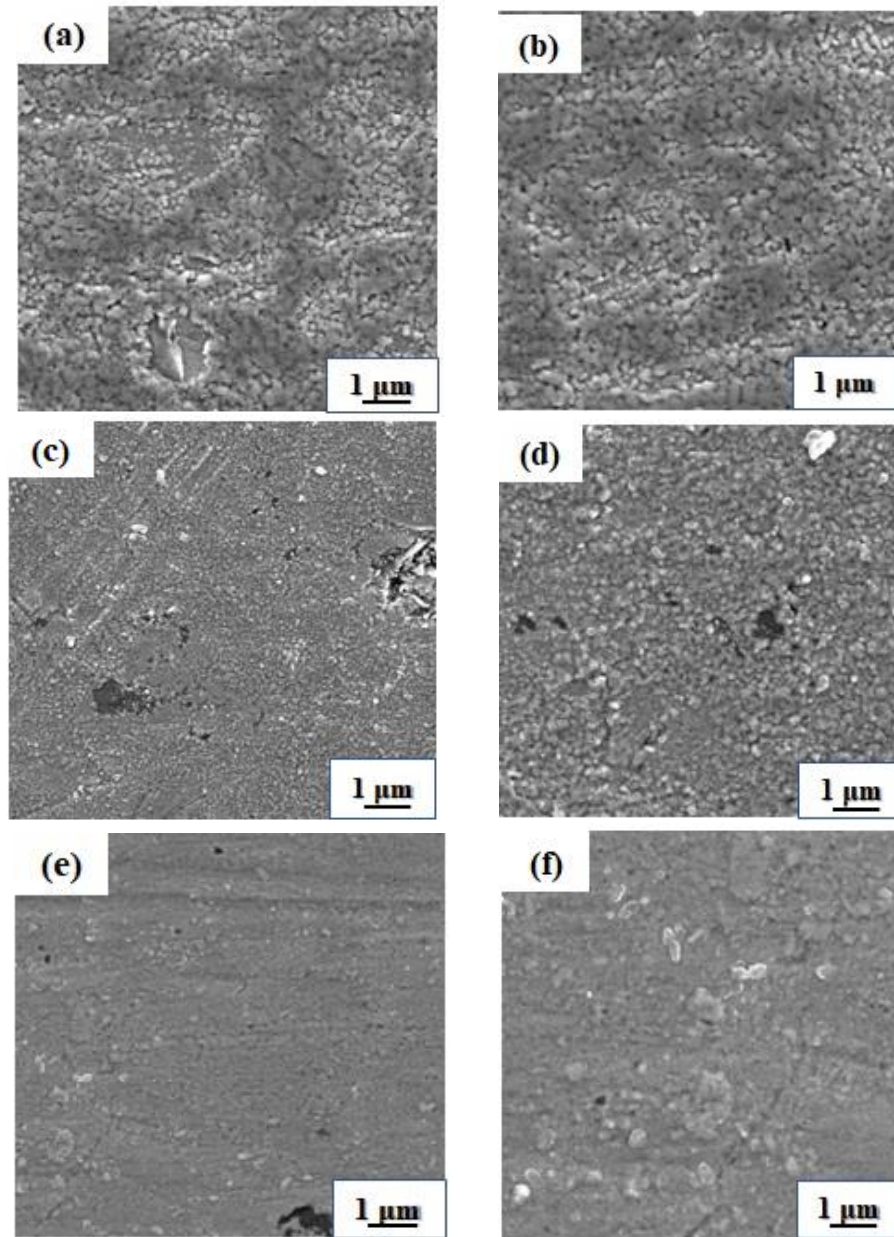

Figure 4.3: Secondary electron images from sample surfaces annealed at 690 °C under: (a) 223 K (-50°C) dp for 60 s, (b) 120 s, (c) 243 K (-30°C) dp for 60 s, (d) 120 s and (e) 268 K (-5°C) dp for 60 s and (f) for 120 s.

It should be noted that at the 223 K (–50°C) dp and 223 K (–30°C) dp process atmosphere, film-like oxides were observed at the surface while increasing the process atmosphere pO_2 through applying the 268 K (–5°C) dp process atmosphere changed the morphology of the oxides to more widely spaced nodule-like particles (Figure 4.3 (e,f))

The fine-scale external and internal oxide microstructural development was studied using TEM. To evaluate the influence of the experimental process atmospheres, samples that were annealed for 120 s under each of the experimental process atmospheres (see Table 4.1) were chosen.

Figure 4.4 depicts high-angle annular dark-field (HAADF) images from cross-sections of samples annealed for 120 s holding time under the 223 K (–50 °C) dp, 243 K (–30°C) dp and 268 K (–5°C) dp process atmospheres. Oxide layers are visible for samples annealed at (–50 °C) and (–30 °C). It can be observed that small oxide particles located in the subsurface formed as internal oxides. For all process atmospheres, direct measurements of the external oxide thicknesses were taken on sample FIB cross-sections and reported as an average of at least 100 observations in Table 4.3. The gray area on top of the images is the Tungsten coating which is followed by a black layer of carbon coating, both deposited on the surface of the sample prior to FIB milling to protect oxides from damage. As it can be seen, Figure 4.4 depicts the 223 K (–50°C) dp sample, an external oxide layer with nonuniform thickness is obvious. On the other hand, no significant internal oxides formed due to the relatively low pO_2 of this process atmosphere which is in the agreement with XPS result (Fig 4.2). At a higher dew point process atmosphere (–30 °C), extensive internal oxidation was detected in addition to a

relatively thick external oxide layer. Figure 4.4 (c) shows sample annealed under (-5°C) dew point process atmosphere which depicts a deeper internal oxidation zone compared to the previous two other dew points. Table 4.3 summarize the average length of internal and external oxidation which were measured by Image J software where the error bars represent the 95 pct confidence interval of the mean.
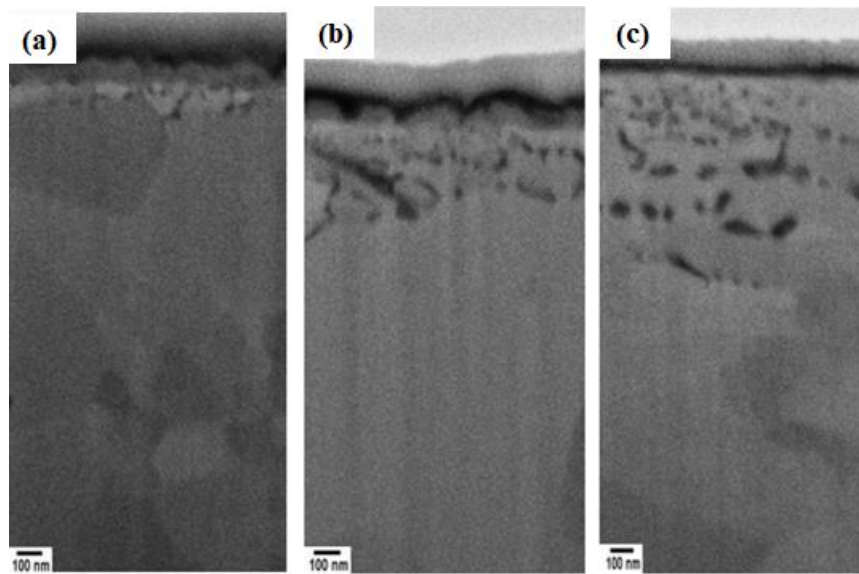
Figure 4.4: HADDF images from the cross-section of samples annealed for 120 s under the (a) (–50°C) process atmosphere, (b) (–30°C) dp process atmosphere (c) (–5 °C) dp process atmosphere.

Table 4.3: Average depth of Internal and External Oxide Thickness.

	(–50 °C) dp	(–30 °C) dp	(–5 °C) dp
External Oxidation 60 s	138±29 nm	119±9 nm	57±8 nm
Internal Oxidation 60 s	33± 7 nm	188± 28 nm	337± 19 nm
External Oxidation 120 s	172± 12 nm	141± 24 nm	93± 11 nm
Internal Oxidation 120 s	41±3 nm	321± 20 nm	455±25 nm

Figure 4.5 shows TEM elemental maps of different elements (O, Mn, Al and Si) at the three process atmosphere dew points for the 120 s IAT. TEM elemental mapping shows that the nodule-like external oxides are Mn-rich while there are not so many Si-rich regions. Therefore, it is concluded that the external oxides are mainly MnO and partly $MnSiO_3$ while at the 268 K (–5°C) dp process atmosphere, external oxides are not significant and significant internal oxides can be seen, especially along the grain boundaries. Thus, most of the oxides formed at this dew point process atmosphere are MnO particles which is in agreement with XPS results (Figure 4.2).

TEM analysis of the annealed steels at three dew point process atmospheres exhibited the existence of a relatively compact layer of external oxides at 223 K (–50°C) dp process atmosphere while the external oxides at higher dew point 243 K (–30°C) dp, began to transit from external to internal oxidation mode. At the highest dew point, the 268 K (–5°C) dp process atmosphere, no compact external oxide layers are visible while internal oxidation especially along grain boundaries are obvious.
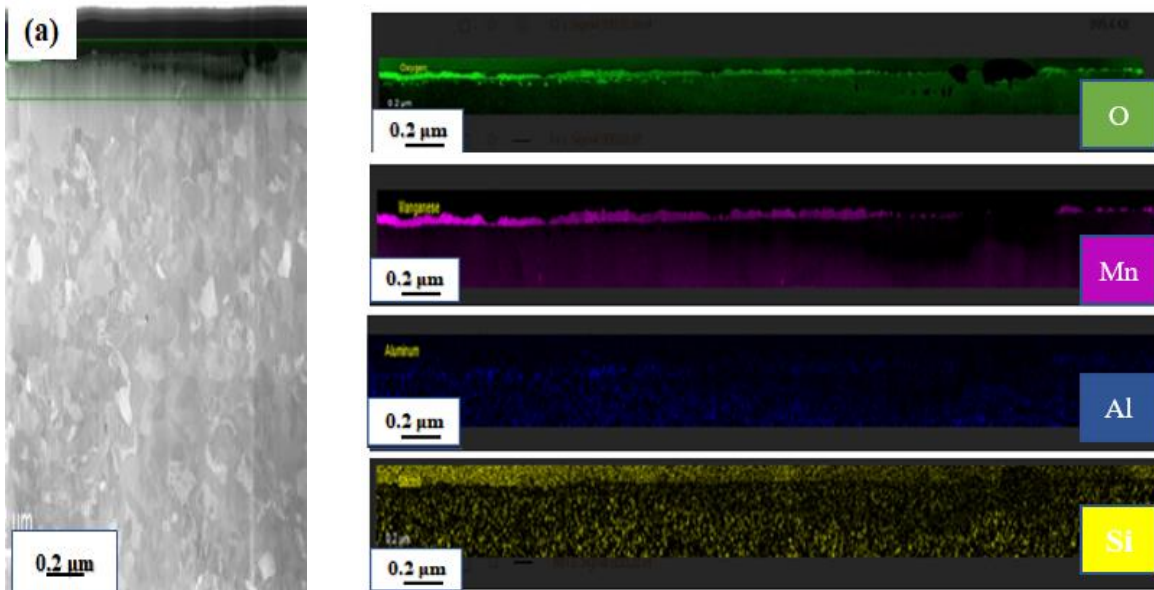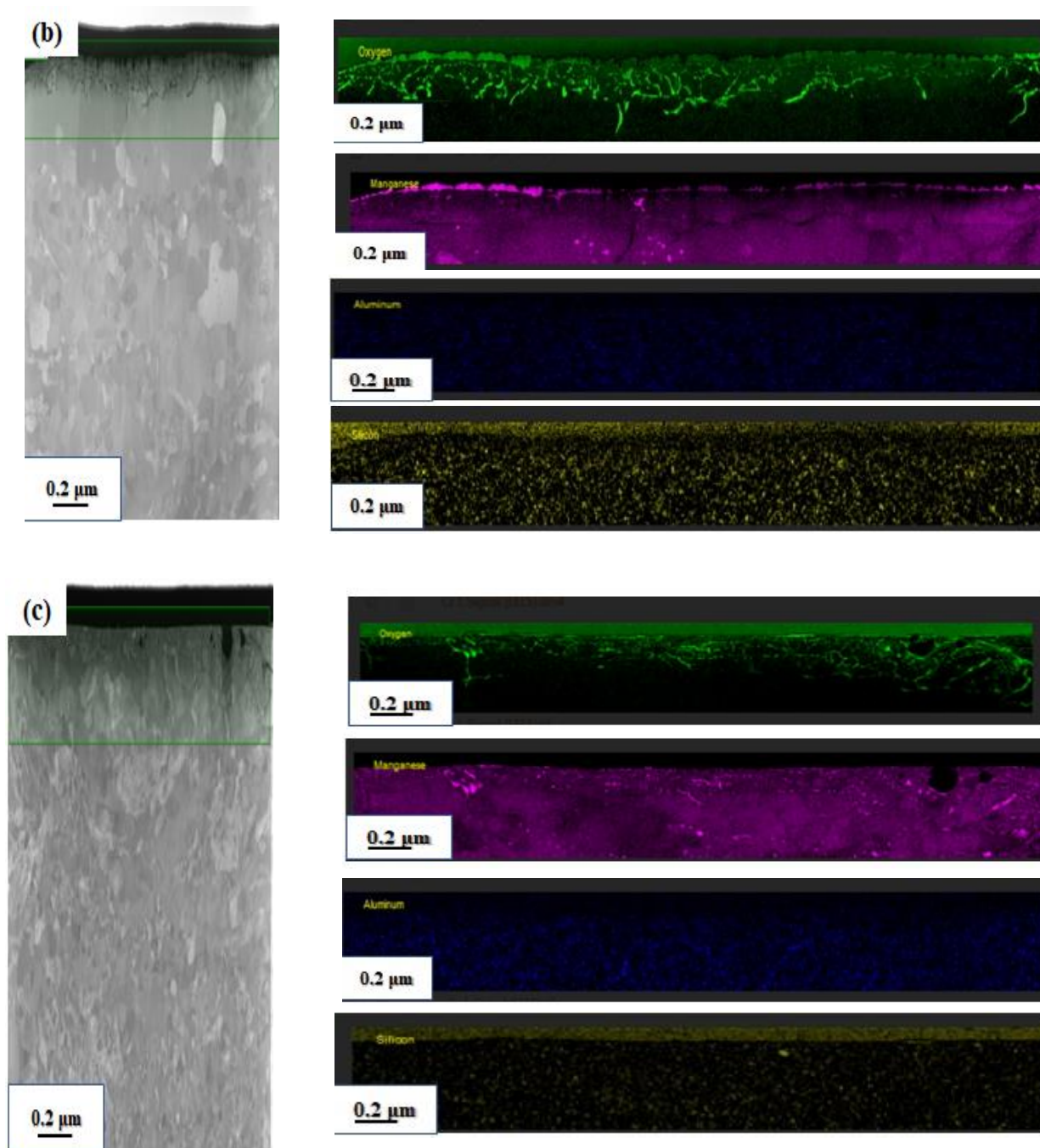
Figure 4.5: TEM elemental maps of samples annealed at 690 °C for 120 s holding time under: (a) 223 K (–50°C) dp, (b) 243 K (–30°C) dp and (c) 268 K (–5°C) dp.

4.2. Reactive wetting

Figure 4.6 depicts a 90 mm × 90 mm uniform temperature and coating areas of the steels annealed under the three-process atmosphere oxygen partial pressures (Table 3.2) and continuously galvanized in the 0.20 wt pct Zn (Al, Fe) bath. It is obvious that even though the steel panel was not coated after being annealed at the lowest pO_2 223 K (–50 °C) dp process atmosphere, increasing the partial oxygen pressure using the 243 K (–30°C) and 268 K (–5°C) dp process atmospheres considerably enhanced the coating quality (Fig 4.6 (c,f)). Depending on the IAT time, there were significant variations in the degree of reactive wetting that occurred. As can be seen in Figure 4.6 (c), despite the existence of some small coating flaws, the substrate surface was fully coated for –30°C dp ×60 s treatment. In contrast to this, no evidence of good reactive wetting for the 120 s holding times was observed (Figure 4.6 (b,d,f)). The best coating with the lowest percentage of bare spot area was observed on the samples annealed under the highest pO_2 268 K (–5 °C) dp process atmosphere as well as 243 K (–30 °C) dp process atmosphere, while, in contrast to this, no integral Zn coating was formed for 223K (–50 °C) dew point. Subsequent analyses and tests were performed on samples whose annealing time was 60 s since they showed the best result under each dew point process atmosphere.
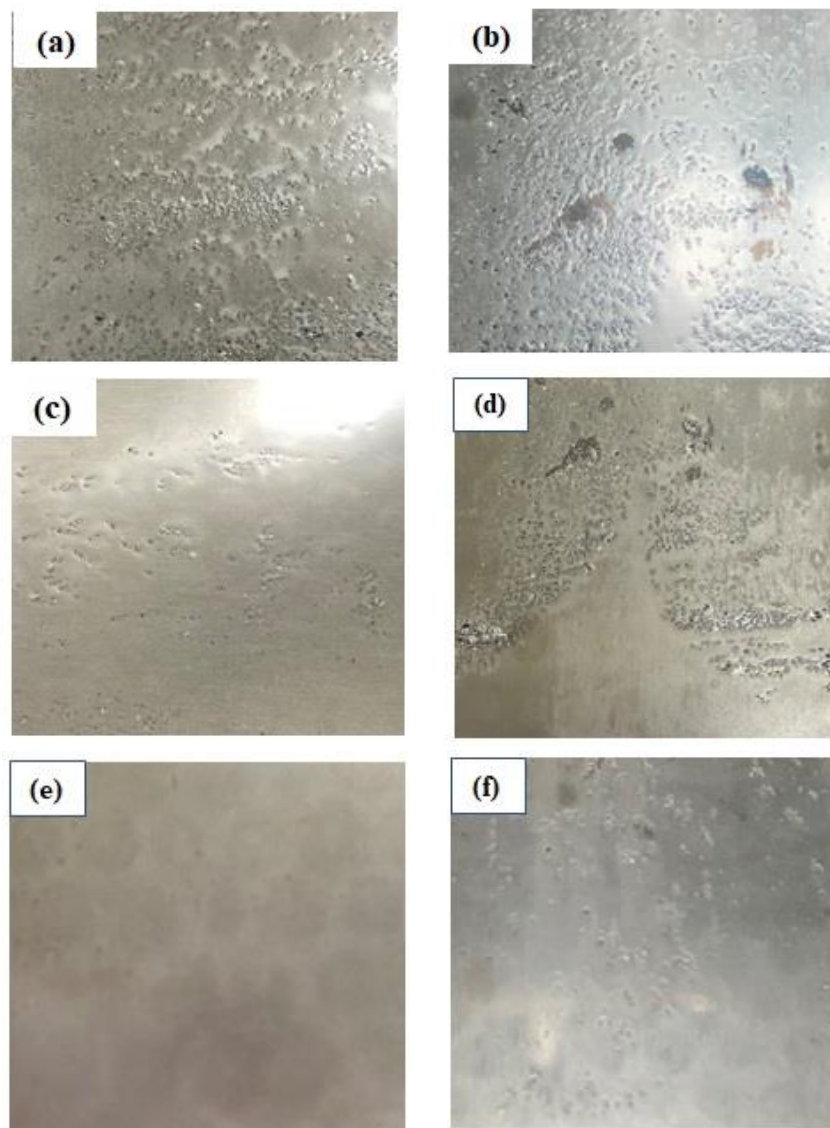
Figure 4.6: Overview of galvanized steel panels as a function of process atmosphere pO_2: (a) 223 K (–50 °C) $\times$ 60 s, (b) 223 K (–50 °C) $\times$120 s, (c) 243 K (–30 °C) $\times$ 60 s and (d) 243 K (–30 °C) $\times$ 120 s, (e) 268 K (–5 °C) $\times$ 60 s and (f) 268 K (–5 °C) $\times$ 120 s.

Three-point bend tests were performed on 10×100 mm^2 strips of the galvanized steels to determine coating adherence and further investigate the coating quality of the galvanized panels. Figure 4.7. shows the galvanized steels' outer radius after being subjected to an ASTM A653/A 653M-05 180° bend test. On the bend test radius, no cracking or flaking could be seen, indicating that the Zn(Al,Fe) coating adherence to the substrate was acceptable under 243 K (–30°C) and268 K (–50°C) dew point process atmosphere, which is turn indicative of good reactive wetting of the as-annealed surface by the galvanizing bath . On the other hand, the surface of sample (a) annealed under 223K (–50 °C) process atmosphere is full of bare spots as well as uncoated areas.
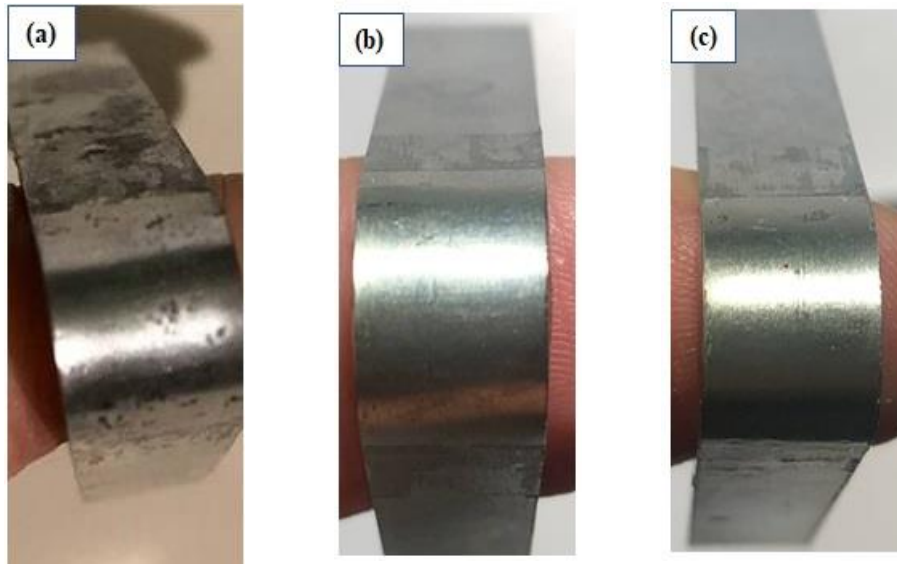
Figure 4.7: ASTM A653/A 653M-05 180° view of the bent area of the galvanized Steel; (a) 223K (–50 °C) × 60 s, (b) 243 K (–30 °C) × 60 s and (c) 268 K (–5 °C) × 60 s.

In order to determine the fine-scale surface coating/steel interfacial morphology of the samples after coating, the as-dipped surfaces were observed under SEM. The zinc overlays were stripped using two solutions: 10 vol% H_2SO_4 (in water) and fuming HNO_3. Figure 4.8. depicts the SEM images of Fe/Zn interfaces being annealed under three atmospheres and 60 s holding time after being stripped with 10vol% H_2SO_4. As previously stated, 10 vol% H_2SO_4-(aq) is used to remove the zinc layer while revealing the interfacial Fe-Zn and Fe-Al intermetallics. For samples annealed under the higher pO_2 243 K (–30 °C) and 268 K (–5 °C) dp process atmosphere, needle-like Fe-Zn (likely ζ-FeZn$_{13}$) intermetallics can be seen. However, for the sample annealed under the 223 K (–50 °C) dp atmosphere, these intermetallics are not as much as higher dew points. It can be observed that increasing the annealing atmosphere pO_2 can lead to the formation of more compact intermetallic crystals at the interface. It can be attributed to localized depletion of Al during aluminothermic reduction of thick oxide layers under low oxygen partial pressures as suggested by Cho et al. [61].
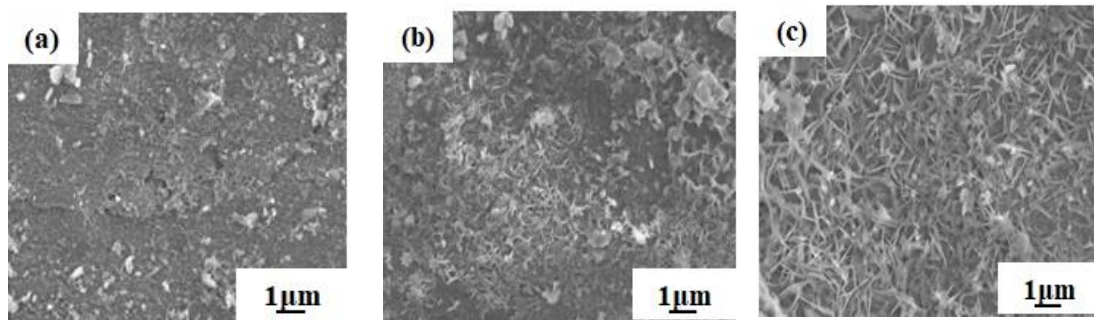
Figure 4.8: Secondary electron images of the coating/steel interface after removal of the top Zn layer with H_2SO_4; (a) 223K (–50 °C), (b) 243 K (–30 °C) and (c) 268 K (–5 °C).

Figure 4.9 shows the SEM images of samples interface annealed under the three process atmospheres, 60 s holding time, and stripped with fuming HNO_3. Equiaxed $Fe_2Al_5Zn_X$ crystals were observed at the Fe/Zn interface of all samples. However, it is obvious, these crystals were formed locally on the surface not uniformly especially under 223 K (–50 °C) dp process atmosphere, indicating some degree of localized reactive wetting under this process atmosphere. As can be seen in Figure 4.9 (b,c), a considerable amount of $Fe_2Al_5Zn_x$ is present at the interface of the samples annealed under the 268 K (–5 °C) and 243 K (–30 °C) process atmospheres, which is in agreement with the good quality of coating showing the occurrence of some reactions between zinc alloy bath and external oxide.
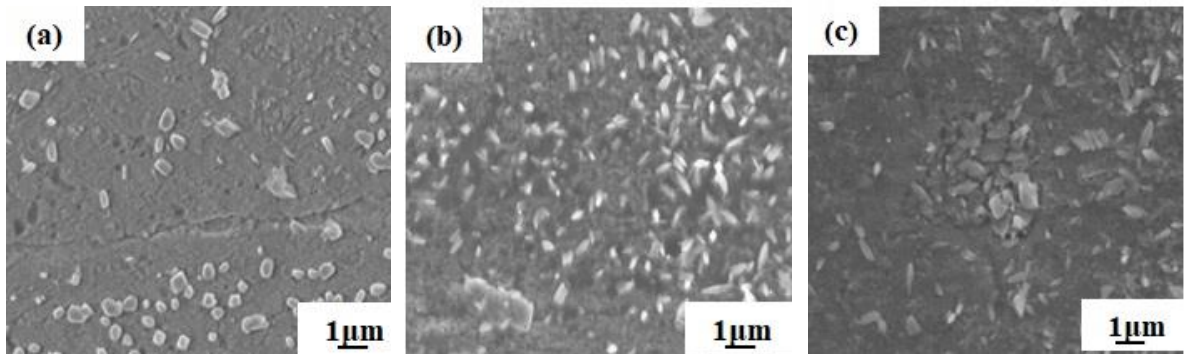
Figure 4.9: Secondary electron images of the coating/steel interface after removal of the top Zn layer with HNO_3; (a) 223 K (–50 °C) dp, and (b) 243K (–30 °C)dp, (c) 268 K (–5 °C)dp.

It can be concluded that under higher process atmosphere pO_2, a well-developed and compact $Fe_2Al_5Zn_x$ will form at the interface. It is worth noting that using the 268 K (–5 °C) dp process atmosphere leads to the interfacial layer developed a fine-grained, more closely packed morphology.

The fine-scale structure of any reaction products at the Fe/Zn interface during galvanizing as well as any changes to the as-annealed oxides after contact with the galvanizing bath was investigated using TEM. Figure 4.10 depicts TEM cross-sectional images along with O, Fe, Si, Mn, Zn and Si EELS elemental maps across the coating/substrate interface taken from three galvanized steels annealed under 223 K (–50 °C) dp, (b) 243 K (–30 °C) dp and (c) 268 K (–5 °C) dewpoint. The surface of the sample annealed under 268 K (–5 °C) was covered with thin, discontinuous MnO oxides while other samples' surfaces were covered with a relatively thick layer of MnO oxides. It should be mentioned that the dark area above the oxides is related to the W film coated on the sample prior to FIB milling.

The galvanized sample under the 268 K (–5 °C) dp atmosphere shows partially reduced MnO oxides since the average thickness of the oxides prior to galvanizing was about 57 nm (Table 4.4) which decreased to 23 nm, indicating that aluminothermic reduction had occurred, which encourages reactive wetting. This effect was not observed in micrographs of the sample annealed under 243 (–30 °C) dp process atmosphere but the surface oxide film showed a broken-up appearance at some sites. Poor reactive wetting of sample annealed under 223 K (–50 °C) dp process atmosphere, in this micrograph, are characterized by the contained voids at the Fe/Zn interface. EELS elemental maps in Figure 4.10 show that the Fe/Zn interface was covered with oxides rich in Mn as well as crystals rich in Al. EELS quantitative point analysis was also done on the sample annealed under 268 K (–5 °C) dewpoint to identify the interfacial reaction products and examine whether the desired $Fe_2Al_5Zn_x$ interfacial has been formed or not.

The results of the analysis are presented in Table 4.4. It was seen that in the vicinity of those areas which showed a strong Al signal, Fe-Al atomic ratios were consistent with the desired $Fe_2Al_5Zn_x$ intermetallic, indicating that reactive wetting has occurred at some sites between the Zn-alloy bath and the substrate which is consistent with the acceptable coating appearance (Figure 4.10 (c)).
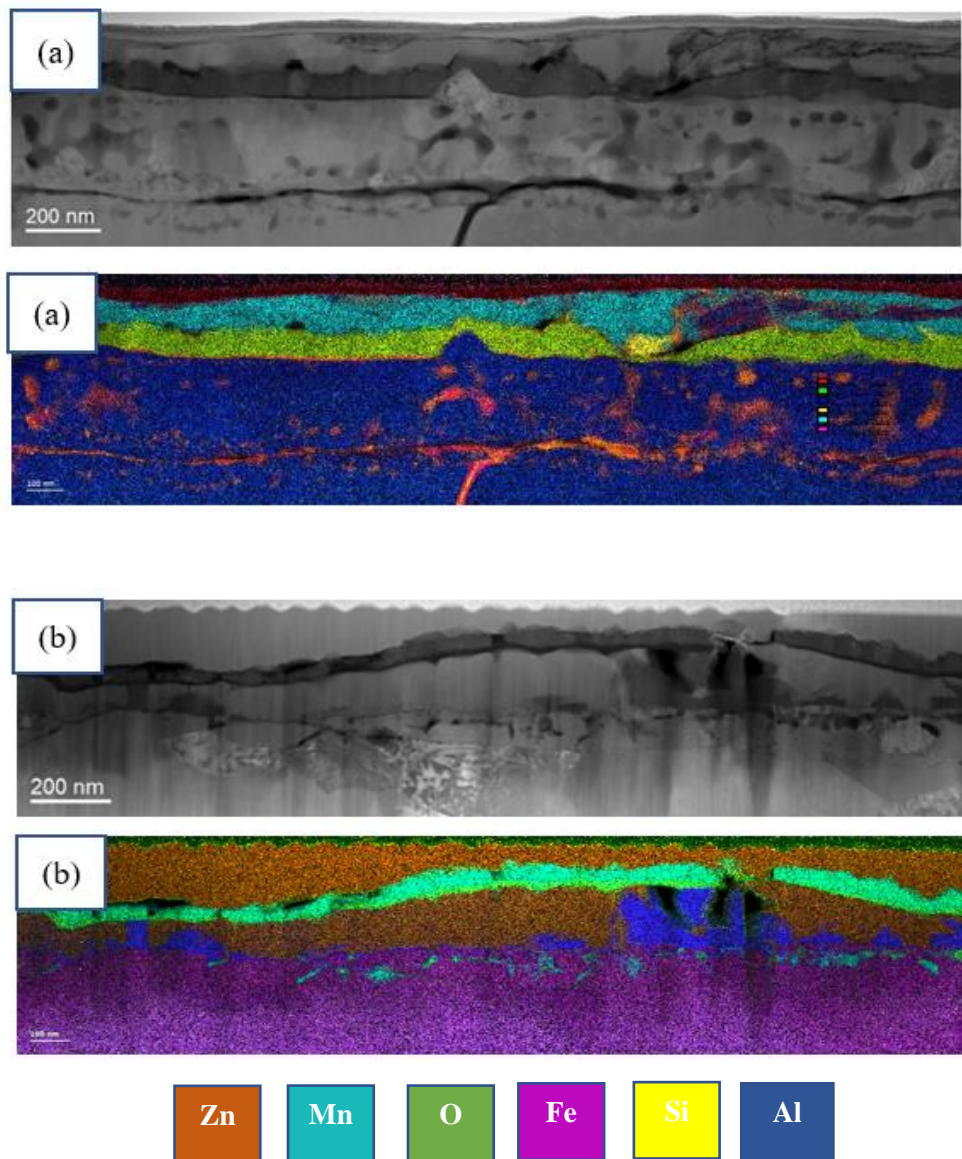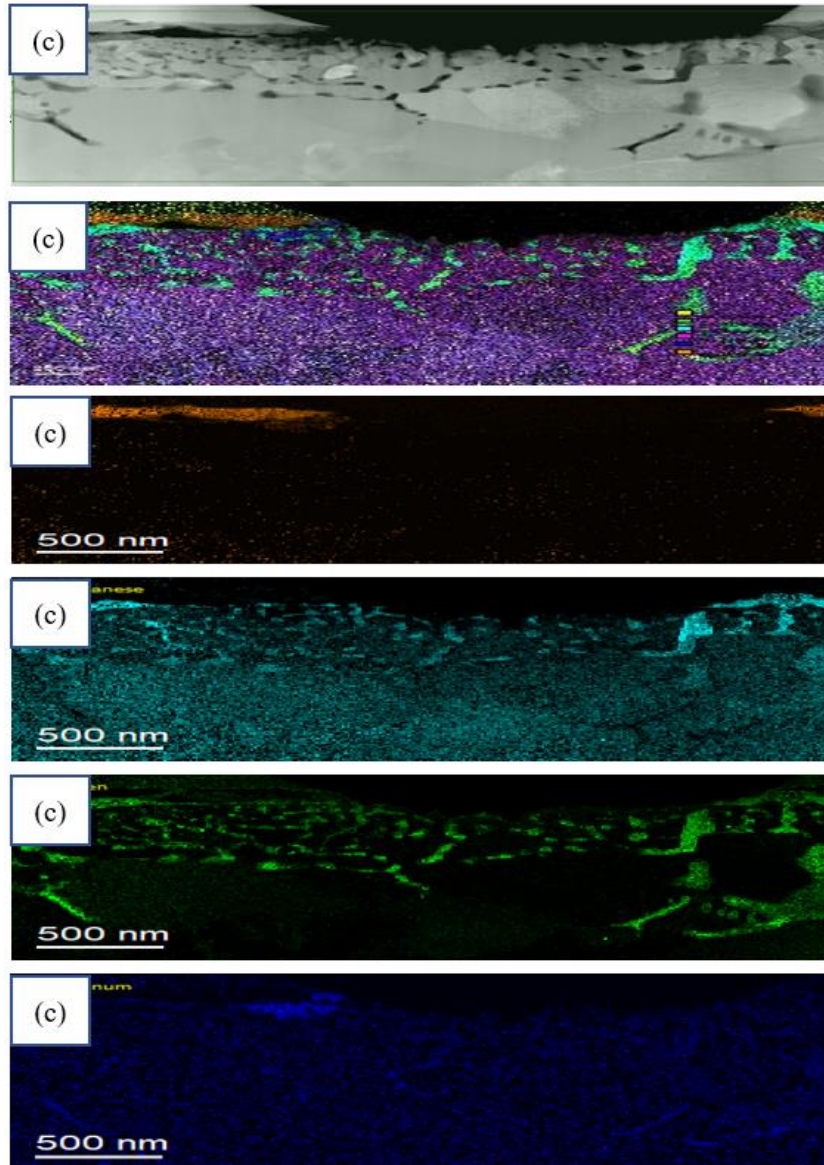
Figure 4.10: TEM cross-sectional micrograph of the coating/substrate interface and subsurface of the galvanized steels of (a) 223 K (–50 °C) dp, (b) 243 (–30 °C) dp and (c) 268 K (–5 °C) dp process atmospheres followed by color over-lay EELS elemental map of the area shown on (a), (b) and (c) and corresponding different elemental maps.
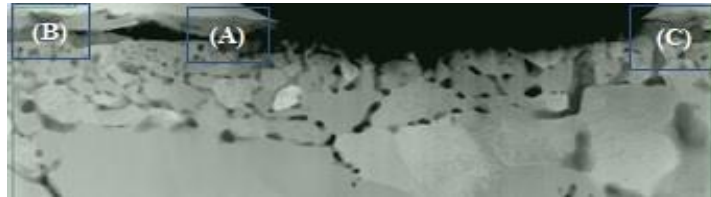
Figure 4.11: TEM cross-sectional and area selected for quantitative point analysis of galvanized sample under 243 (–5 °C) dp process atmosphere.

Table 4.4: Quantitative EELS analysis results corresponding to area A to C in Figure 4.11(at%)

Area	Zn	Al	Mn	O	Fe	Si	Phase Present
A	8.5	54.3	2.2	8.4	25.4	1.2	$Fe_2Al_5Zn_x$
B	1.4	23.7	39.3	25.8	8.0	1.8	Mn oxide
C	58.6	3.4	8.9	10.2	18.5	0.4	Zn alloy

Chapter 5: Discussion

Based on the Wagner bulk and grain boundaries model for calculation of the selective oxidation of Mn and Si in the present experimental alloy at 963 K (690 °C) in a N_2-5 vol.% H_2, it was concluded that the predictions (Table 4.1) match well with XPS (Fig. 4.2) and TEM results and measurements (Fig. 4.5), indicating that the predicted external oxidation mode for Mn under all dewpoints atmospheres is correct. Moreover, in the 268 K (–5 °C) process atmosphere, the anticipated internal oxidation mode for Mn (Fig. 4.1) was found to be compatible with TEM and XPS data, the latter of which showed the concentration of Mn above the bulk composition well below the substrate surface as well as the reduced surface enrichment (Fig 4.2). The subsurface peaks (Figure 4.2) in the Mn XPS profiles for the 268 K (–5 °C) process atmosphere give some evidence for internal oxidation since these localized peaks likely came from either the bulk or grain boundary internal oxides. For the lowest pO_2 223 K (–50 °C) dp process atmosphere (Table 4.1) both Si and Mn were predicted to oxidize externally in the bulk ferrite and along its grain boundaries, which is consistent with the XPS (Fig. 4.2 (a,b)). According to the Wagner model [103], for the intermediate pO_2 243 K (–30°C) dp process atmosphere (Table 4.1), both Mn and Si were predicted to oxidize externally in the bulk ferrite (Fig.) while XPS, SEM, and TEM observations showed that Mn oxidized internally in the bulk (Fig 4.3, 4.5). This disagreement can originate from either the limitations of Mn and Si diffusivity data, the proximity of the predicted internal/external transition to the experimental conditions or, a combination of both.

The oxidation potential of the annealing atmosphere has a substantial influence on the surface oxide morphology and distribution, as shown by SEM micrographs in Figures 4.3. The outermost external oxide layer for all process atmospheres was found to be MnO, as established by XPS binding energy data (Table 4.2) and TEM+EELS analysis (Fig. 4.4, 4.5). Annealing under the 268 k (–5°C) dp process atmosphere resulted in an increase in the surface area fraction not occupied by MnO nodules or films whereas the highest surface coverage by external MnO was observed under 223 K (–50°C) dp process atmosphere, indicating that the process atmosphere's oxidation potential highly influenced the oxide morphology. It should be noted that under the 223 K (–50°C) dp and 223 K (–30°C) dp process atmosphere, film-like oxides were observed at the surface while increasing the process atmosphere pO_2 through applying the 268 K (–5°C) dp process atmosphere changed the morphology of the oxides to more widely spaced nodule-like particles (Figure 4.3 (e,f)). Further increasing the process atmosphere pO_2 using the 268 k (–5°C) dp process resulted in a significant reduction in surface coverage (Fig 4.3 e,f) which is in agreement with the XPS results (Fig 4.2) and the external to internal oxidation transition predicted by Wagner model [103]. On the other hand, it was observed that by increasing the annealing period to 120 s, the oxide cluster expanded and the full coverage of the surface by oxides occurred.

Based on the XPS results, Manganese showed significant surface enrichment compared to the bulk concentrations for the lowest pO_2 process atmosphere (223 k (–50 °C)) dp, which quickly dropped with increasing depth to values close to the nominal bulk

concentration of each element. Increasing the annealing holding time from 60 s to 120 s leads to an increase in the external oxide layer which is shown in Figures 4.2 (a) and (b). The restriction of the enrichment zone to the outer surface indicates an external oxidation mode, which is consistent with the Wagner model prediction for Manganese (Table 4.1). Therefore, it can be inferred from Figure 4.2 (a,b) that the thickness of the external MnO for both steel samples annealed under (–50 °C) and (–30 °C) increased with increasing annealing time for the mentioned dew points (138 nm and 119 nm, respectively). It can also be observed that the depth of internal oxidation rose when the annealing time was increased from 60 s to 120 s as a result of the diffusion-driven process.

By comparing the obtained XPS binding energies, the oxides were identified. Under the annealing atmospheres used in this study, thermodynamic calculations clearly reveal that MnO, SiO_2, $MnSiO_3$, and Mn_2SiO_4 produce stable oxides (Table 4.2). The morphology and formation mode (internal or exterior) of these oxides, on the other hand, are both influenced by kinetic factors such as the relative diffusion rates of Mn, Si, and O. Using a high dew point or high pO_2 atmosphere during AHSS annealing has been considered to be a potential approach for promoting internal selective oxidation of ignoble alloying elements and reactive wetting of these more highly alloyed steels during continuous galvanizing [63]. As demonstrated by Bellhouse and McDermid [64], surfaces that were relatively free of external oxides or covered with thinner oxide films can be reactively wetted by the Zn(Al, Fe) bath. This occurs since external oxides function as a barrier between the Zn(Al, Fe) bath and the iron substrate which results in preventing iron

dissolution reaction needed to form the intended $Fe_2Al_5Zn_x$ interfacial layer at the substrate/coating interface.

According to the results of this study experiments, utilizing a process atmosphere pO_2 that encourages internal oxidation; in this research the 243 K (–30 °C) and 268 K (–5 °C) dp process atmospheres and 60 s holding time are considered to be more beneficial in boosting reactive wetting of the experimental substrate compared to the lower pO_2 223 K (–50 °C) dp process atmosphere. This benefit originates from the surface oxide morphology which consists of thin films or widely spaced nodules. Furthermore, external MnO and Mn-Si mixed oxides have been shown to produce fewer reactive wetting issues than SiO_2 which was negligible on the surface in this study because MnO and Mn-Si mixed oxides have been suggested to be partially reduced due to aluminothermic reduction during galvanizing [104,105] and bath infiltration along cracks at the metal/oxide interface. Therefore, the steel strip will be in contact with zinc bath, creating favorable conditions for the Fe-Al interfacial layer to develop. However, the kinetics of aluminothermic reduction dictate its efficacy in assisting reactive wetting, since the aluminothermic reduction of MnO by dissolved Al in CGL solution is limited by the oxide thickness for a particular set of annealing temperatures.

Figure 4.6 shows that the experimental steel annealed under the lowest pO_2 223 K (–50 °C) dp process atmosphere had weak reactive wettings, as can be observed that no well-developed, integral Fe-Al interfacial layer formed at the Fe/Zn interface, as shown in Figure (4.9 (a)). This is due to the thickness and morphology of the external oxides produced on the surface during annealing prior to galvanizing (Fig. 4.3). It was

measured that under 223 K (–50 °C) dp process atmosphere, a compact 138 nm-thick film-like oxide formed on the external surface prior to galvanizing. These oxides act as a barrier to the dissolution of Fe from the substrate which prevents the desired reaction of dissolved Fe, Zn, and Al to form the $Fe_2Al_5Zn_x$ layer at the interface.

According to Sagl et al. [106], close to the surface areas covered with thinner oxide layers and nodule-like oxide particles, where Fe dissolution in the zinc bath and formation of the $Fe_2Al_5Zn_x$ crystals is feasible, oxides can lose their adherence to the substrate and lift off in the bath and trapped within $Fe_2Al_5Zn_x$ crystals as they grow. However, this mechanism was not observed in this study.

Employing a higher dew point process atmosphere during annealing the substrate has been proven to enhance reactive wetting by boosting internal selective oxidation of alloying elements as characterized by the Wagner model for the internal to external oxidation transition. Boosting of internal oxidation often results in thin oxide films and widely spaced, distinct nodule-like external oxides which have been established to promote reactive wetting.

Samples annealed under 243 (–30 °C) K and 268 K (–5 °C) dew points process atmospheres exhibited fairly good reactive wetting as the low number and small area of bare spots in the Zn overlay as well as no cracking or flaking of the coating during bend testing. This can be attributed to the formation of thin layers of oxides on the surface of steels as a result of the transition from external to internal oxidation. Another reason could be spalling and cracking of the oxide which can happen upon cooling from

the IAT, as the result of the difference in coefficient of thermal expansion between the substrate and the oxides as suggested by McDermid [64]. These cracks could allow bath liquid infiltration and direct contact with the substrate as can be seen in Figure (4.10 (b)), resulting in Fe dissolution from substrate and the precipitation of $Fe_2Al_5Zn_x$ crystals between and below the oxides.

The best reactive wetting obtained for the steel annealed under 268 K (–5 °C) dp process atmosphere. It can be explained by the morphology of the external oxides. As discussed, by increasing the process atmosphere pO_2 to 268 K (–5 °C) dp changed the morphology of the surface oxides from film-like to more widely-spaced oxides (Fig. 4.3). This morphology could enhance aluminothermic reduction of oxides and dissolution of Fe into the galvanizing bath which results in the formation of a continuous desired $Fe_2Al_5Zn_x$ interfacial layer and fewer bare spots compared to the lower pO_2 dewpoints atmospheres in this study. This mechanism is in agreement with Belhouse and McDermid [64] findings which relates the formation of a homogeneous the $Fe_2Al_5Zn_x$ layer after hot-dip galvanizing a TRIP steel to widely spaced oxide nodules with relatively thin nodular MnO films resulting from higher pO_2 268 K (–5 °C) dp process atmosphere compared to lower pO_2.

It should be noted, however, that substantial work in the direction of kinetically-based modeling of both external and internal oxidation has been done, beginning with Huin et al. [82] and continuing with Brunac et al., Lashgari et al., and Leblond et al. [107]. When compared to the current experimental data, these models have proved to be more accurate compared to simply thermodynamic-based models. These

models showed better agreement with the current experimental data. However, because external oxide morphology plays such a dominant role in determining the interactions between as-annealed substrate surfaces and the continuous galvanizing bath, as well as the final quality of reactive wetting, progress in the modeling of selective oxidation to include the development of external and internal oxide morphology in addition to thermodynamic and kinetic is critical. These attempts will provide a substantial challenge to the continuously galvanizing research community moving forward.

Chapter 6: Conclusions

Under the 223 K (–50 °C) dp process atmosphere, a compact, thick, film-like oxide comprising mostly Mno as well as $MnSiO_3$ and Mn_2SiO_4, oxides, covered the surface while internal oxidation was insignificant.

Increasing the process atmosphere pO_2 by using the 243 K (–30 °C) dp resulted in a transition from external to internal selective oxidation and led tonthe formation of oxides both on the surface and in the subsurface. Film-like external oxides were identified to be a mixture of MnO, $MnSiO_3$ and Mn_2SiO_4.

Further increasing the atmosphere pO_2 by employing the 268 K (–5 °C) dp process atmosphere altered the morphology of the external oxides from film-like for the 223 K (–50 °C) and 243 K (–30°C) dp process atmospheres to discrete nodule-like particles. The external oxides were identified as MnO and mixture of $MnSiO_3$ and Mn_2SiO_4. The internal oxides depth increased significantly compared to previous process atmosphere dewpoints.

The external oxides present for all annealing temperatures and times were composed of MnO, as confirmed by both XPS and TEM+EELS analyses. However, a considerable increase in the surface Mn enrichment was observed with increasing the intercritical annealing time from 60 s to 120 s. Holding the experimental steel at the intercritical annealing temperature for longer times led to an increase in either the thickness of the external oxides or depth of internal oxidation.

Successful reactive wetting of the 268 K (–5 °C) dp process atmosphere substrate by the Zn-0.20 wt% Al (dissolved) galvanizing bath was due to the finer morphology and wider spacing of nodules formed at the surface during annealing. Mechanisms such as aluminothermic reduction of MnO oxides resulted in a better coating compared to other dewpoints, while, in contrast, poor reactive wetting was seen for 223 K (–50 °C) dp process atmosphere sample which was attributed to the surface structure that was fully covered with a compact, coarse and 138 nm-thick oxide layer which did not allow the contact between the underlaying substrate and the bath alloy which resulted in preventing Fe dissolution and precipitation of the desired $Fe_2Al_5Zn_x$.

Chapter 7: References

[1] E. De Moor, P. J. Gibbs, J. G. Speer, D. K. Matlock, and J. G. Schroth, "AIST transactions strategies for third-generation advanced high-strength steel development," Iron steel Technol., vol. 7, no. 11, p. 132, 2010.

[2] Jin, Xinyan; Hu, Guangkui; Wang, Li; Wang, Hua (2019). Characterization of surface layers of oxidation-reduction treated Si and Mn added advanced high strength steel. Surface and Coatings Technology, 125172–. doi:10.1016/j.surfcoat.2019.125172

[3] D. K. Matlock and J. G. Speer, "Design considerations for the next generation of advanced high strength sheet steels," in Proc. of the 3rd International Conference on Structural Steels, ed. by HC Lee, the Korean Institute of Metals and Materials, Seoul/Korea, 2006, pp. 774–781.

[4] M.J. Merwin: Mater. Sci. Forum, 2007, vol. 539, pp. 4327–30.

[5] "2019 Volvo XC90 - Luxury SUV | Volvo Car USA."

[6] Zhang, Xue; da Silva, Cau CorrAa; Liu, Chang; Prabhakar, Manoj; Rohwerder, Michael (2020). Selective oxidation of ternary Fe-Mn-Si alloys during annealing process. Corrosion Science, (), 108859–. doi:10.1016/j.corsci.2020.108859

[7] P. Tsipouridis, "Mechanical properties of dual-phase steels", PhD thesis, Technischen Universitat Munchen (2006).

[8] S. Lee, S. Shin, M. Kwon, K. Lee, and B. C. De Cooman, "Tensile Properties of Medium Mn Steel with a Bimodal UFG α + γ and Coarse δ-Ferrite Microstructure," Metall. Mater. Trans. A, vol. 48, no. 4, pp. 1678–1700, Apr. 2017.

[9] D. K. Matlock and J. G. Speer, "Third Generation of AHSS: Microstructure Design Concepts," in Microstructure and Texture in Steels, London: Springer London, 2009, pp. 185–205.

[10] Yang, Tong; He, Yanlin; Chen, Zhang; Zheng, Weisen; Wang, Hua; Li, Lin (2020). Effect of Dew Point and Alloy Composition on Reactive Wetting of Hot Dip Galvanized Medium Manganese Lightweight Steel. Coatings, 10(1), 37–. doi:10.3390/coatings10010037

[11] C. Schutte, "SAE Technical Paper 2015-01-0405." 2015.

[12] Zapico-Alvarez, David; Barges, Patrick; Musik, Celine; Bertrand, Florence; Mataigne, Jean-Michel; Descoins, Marion; Mangelinck, Dominique; Giorgi, Marie-Laurence (2020). Further Insight into Interfacial Interactions in Iron/Liquid Zn-Al System. Metallurgical and Materials Transactions A, (), –. doi:10.1007/s11661-020-05669-5.

[13] K. Steineder, D. Krizan, R. Schneider, C. Béal, and C. Sommitsch, "On the microstructural characteristics influencing the yielding behavior of ultra-fine grained medium-Mn steels," Acta Mater., vol. 139, pp. 40–50, Oct. 2017.

[14] D. Lee, J.-K. Kim, S. Lee, K. Lee, and B. C. De Cooman, "Microstructures and mechanical properties of Ti and Mo micro-alloyed medium Mn steel," Mater. Sci. Eng. A, vol. 706, pp. 1–11, Oct. 2017.

[15] M. Pourmajidian and J. R. Mcdermid, "Effect of Annealing Temperature on the Selective Oxidation and Reactive Wetting of a 0.1C-6Mn-2Si Advanced High Strength Steel During Continuous Galvanizing Heat Treatments," ISIJ Int., vol. 58, no. 9, pp. 1635–1643, Sep. 2018.

[16] J.M. Mataigne, M. Lamberigts, V. Leroy (1992) "Developments in the Annealing of Sheet Steels".

[17] G. Seyed Mousavi, J.R. McDermid, in Int. Conf. Zinc Zinc Alloy Coat. Steel Sheet, Tokyo (2017) 486–92.

[18] M. Pourmajidian and J. R. McDermid, "Selective Oxidation of a 0.1C-6Mn-2Si Third Generation Advanced High-Strength Steel During Dew-Point Controlled Annealing," Metall. Mater. Trans. A, vol. 49, no. 5, pp. 1795–1808, May 2018.

[19] J. Mahieu, B. C. De Cooman, and S. Claessens, "Galvanizability of high-strength steels for automotive applications," Metall. Mater. Trans. A, vol. 32, no. 11, pp. 2905–2908, Nov. 2001

[20] S. Alibeigi, "Short-term formation kinetics of the continuous galvanizing interfacial layer on Mn-containing steels", PhD thesis, McMaster University (2014).

[21] E. De Moor, P. J. Gibbs, J. G. Speer, and D. K. Matlock, "Strategies for ThirdGeneration Advanced High-Strength Steel Development," AIST Trans., vol. 7, no. 3, pp. 133–144, 2010.

[22] Jacques et al. 2001, Merwin 2007, Matlock and Speer 2009, McDermid et al. 2011.

[23] J. Jun and N. Fonstein, "Microstructure and Tensile Properties of TRIP -Aided CR Sheet Steels: TRIP, Dual and Q&P," in Proceedings of the International Conference on New Developments in Advanced High-Strength Sheet Steels, 2008, pp. 155–168

[24] A. K. Sachdev, "Effect of Retained Austenite on the Yielding and Deformation Behavior of a Dual Phase Steel," Acta Metall., vol. 31, no. 12, pp. 2037–2042, 1983.

[25] M. J. Merwin, "Low-Carbon Manganese TRIP Steels," Mater. Sci. Forum, vol. 539–543, pp. 4327–4332, 2007.

[26] R. Kavitha and J. R. McDermid, "On the in-situ aluminothermic reduction of manganese oxides in continuous galvanizing baths," Surf. Coat. Technol., vol. 212, pp. 152–158, 2012.

[27] G. Thomas, J. G. Speer, D. K. Matlock, and E. De Moor, "Alloy Design for Fundamental Study of Quenched and Partitioned Steels," in MS&T 2011 Conference Proceedings, 2011, pp. 552–567.

[28] F. G. Caballero, J. Chao, J. Cornide, C. Garcia-Mateo, M. J. Santofimia, and C. Capdevila, "Toughness deterioration in advanced high strength bainitic steels," Mater. Sci. Eng. A, vol. 525, pp. 87–95, 2009.

[29] W. Steven and A. G. Haynes, "The Temperature Formation of Martensite and Bainite in Alloy Steels - Some Effects of Chemical Composition," J. Iron Steel Inst., vol. 183, pp. 349–359, 1956.

[30] A. K. Sachdev, "Effect of Retained Austenite on the Yielding and Deformation Behavior of a Dual Phase Steel," Acta Metall., vol. 31, no. 12, pp. 2037–2042, 1983.

[31] C. Garcia-Mateo and F. G. Caballero, "Ultra-high–strength Bainitic Steels," ISIJ Int., vol. 45, no. 11, pp. 1736–1740, 2005.

[32] F. G. Caballero and C. Garcia-Mateo, "The Role of Retained Austenite on Tensile Properties of Steels with Bainitic Microstructures," Mater. Trans., vol. 46, no. 8, pp. 1839– 1846, 2005.

[33] J. Jun and N. Fonstein, "Microstructure and Tensile Properties of TRIP -Aided CR Sheet Steels: TRIP, Dual and Q&P," in Proceedings of the International Conference on New Developments in Advanced High-Strength Sheet Steels, 2008, pp. 140–160.

[34] W. Steven and A. G. Haynes, "The Temperature Formation of Martensite and Bainite in Alloy Steels - Some Effects of Chemical Composition," J. Iron Steel Inst., vol. 183, pp. 349–359, 1956.

[35] M. Calcagnotto, D. Ponge, and D. Raabe, "Effect of grain refinement to 1 um on strength and toughness of dual-phase steels," Mater. Sci. Eng. A, vol. 527, no. 29–30, pp. 7832– 7840, 2010.

[36] K. Sugimoto, T. Iida, J. Sakaguchi, and T. Kashima, "Retained Austenite Characteristics and Tensile Properties in a TRIP Type Bainitic Sheet Steel," ISIJ Int., vol. 40, no. 9, pp. 902–908, 2000.

[37] M. De Meyer, D. Vandershueren, and B. C. De Cooman, "The Influence of Substitution of Si by Al on the Properties of Cold Rolled C-Mn-Si TRIP Steels," ISIJ Int., vol. 39, no. 8, pp. 813– 822, 1999.

[38] J. Mahieu, J. Maki, B. C. De Cooman, and S. Claessens, "Phase Transformation and Mechanical Properties of Si-Free CMnAl Transformation-Induced Plasticity-Aided Steel," Metall. Mater. Trans. A, vol. 33, no. 8, pp. 2573–2580, 2002.

[39] R. L. Bodnar, T. Ohhashi, and R. I. Jaffee, "Effects of Mn, Si and Purity on the Design of 3.5NiCrMoV, 1CrMoV, and 2.25Cr-1Mo Baintic Alloy Steels," Metall. Mater. Trans. A, vol. 20, no. 8, pp. 1445–1460, 1989.

[40] O. Matsumura, Y. Sakuma, and H. Takechi, "Enhancement of Elongation by Retained Austenite in Intercritical Annealed 0.4C-1.5Si-0.8Mn Steel," Trans. ISIJ, vol. 27, pp. 570– 579, 1987.

[41] O. Matsumura, Y. Sakuma, Y. Ishii, and J. Zhao, "Effect of Retained Austenite on Formability of High Strength Sheet Steels," ISIJ Int., vol. 32, no. 10, pp. 1110–1116, 1992.

[42] A. J. Clarke, J. G. Speer, M. K. Miller, R. E. Hackenberg, D. V. Edmonds, D. K. Matlock, F. C. Rizzo, K. D. Clarke, and E. De Moor, "Carbon partitioning to austenite from martensite or bainite during the quench and partition (Q&P) process: A critical assessment," Acta Mater., vol. 56, no. 1, pp. 16–22, 2008.

[43] J. Speer, D. K. Matlock, B. C. De Cooman, and J. G. Schroth, "Carbon partitioning into austenite after martensite transformation," Acta Mater., vol. 51, no. 9, pp. 2611–2622, 2003.

[44] G. A. Thomas and J. F. Hansman, "Development, Design, and Industrial Launch of Next-Generation Steel," in International Symposium on New Developments in Advanced HighStrength Sheet Steels, 2017, pp. 11–18.

[45] R. A. Grange and H. M. Stewart, "The Temperature Range of Martensite Formation," Trans. AIME, vol. 167, pp. 467–490, 1946.

[46] R. A. Grange and R. L. Miller, "Heat Treatment for Improving the Toughness of High Manganese Steels,".

[47] R. L. Miller, "Ultrafine-Grained Microstructures and Mechanical Properties of Alloy Steels," Metall. Trans., vol. 3, no. April, pp. 905–912, 1972.

[48] M. J. Merwin, "Low-Carbon Manganese TRIP Steels," Mater. Sci. Forum, vol. 539–543, pp. 4327–4332, 2007.

[49] M. J. Merwin, "Microstructure and Properties of Cold Rolled and Annealed Low-Carbon Manganese TRIP Steels," Iron Steel Technol., vol. 5, no. 10, pp. 66–84, 2008.

[50] P. J. Gibbs, E. De Moor, M. J. Merwin, B. Clausen, J. G. Speer, and D. K. Matlock, "Austenite stability effects on tensile behavior of manganese-enriched- austenite transformation-induced plasticity steel," Metall. Mater. Trans. A Phys. Metall. Mater. Sci., vol. 42, no. 12, pp. 3691–3702, 2011.

[51] Manna, M.; Dutta, M.; Bhagat, A. N. (2020). "Microstructure and Electrochemical Performance Evaluation of Zn, Zn-5 wt.% Al and Zn-20 wt.% Al Alloy Coated Steels", Journal of Materials Engineering and Performance, (134), 2020.

[52] J. Mahieu, J. Maki, B. C. De Cooman, and S. Claessens, "Phase Transformation and Mechanical Properties of Si-Free CMnAl Transformation-Induced Plasticity-Aided Steel," Metall. Mater. Trans. A, vol. 33, no. 8, pp. 2573–2580, 2002.

[53] W. Steven and A. G. Haynes, "The Temperature Formation of Martensite and Bainite in Alloy Steels - Some Effects of Chemical Composition," J. Iron Steel Inst., vol. 183, pp. 349–359, 1956.

[54] H. Hofmann, D. Mattissen, and T. W. Schaumann, "Advanced Cold Rolled Steels for Automotive Applications," Steel Res. Int., vol. 80, no. 1, pp. 22–28, 2009.

[55] D. Huin, P. Flauder, and J. B. Leblond, "Numerical Simulation of Internal Oxidation of Steels during Annealing Treatments," Oxid. Met., vol. 64, pp. 131–167, 2005.

[56] V. A. Lashgari, C. Kwakernaak, and W. G. Sloof, "Transition from Internal to External Oxidation of Mn Steel Alloys," Oxid. Met., vol. 81, pp. 435–451, 2014.

[57] M. Pourmajidian and J. R. McDermid, "Effect of Annealing Temperature on the Selective Oxidation and Reactive Wetting of a 0.1C-6Mn-2Si Advanced High Strength Steel During Continuous Galvanizing Heat Treatments," ISIJ Int., vol. 58, no. 9, pp. 1635–1643, Sep. 2018.

[58] Pallisco, Daniella M.; McDermid, Joseph R. (2020). Mechanical property development of a 0.15C-6Mn-2Al-1Si third-generation advanced high strength steel using continuous galvanizing.Materials Science: A, 778(), 139111–. doi:10.1016/j.msea.2020.139111

[59] A. Ruck, D. Monceau, and H. J. Grabke, "Effects of tramp elements Cu, P, Pb, Sb and Sn on the kinetics of carburization of case hardening steels," Steel Res. Int., vol. 67, no. 6, pp. 240–246, 1996.

[60] J. Oh, L. Cho, M. S. Kim, K. Kang, and B. C. De Cooman, "The Effect of Bi on the Selective Oxide Formation on CMnSi TRIP Steel," Metall. Mater. Trans. A, vol. 47, no. 11, pp. 5474– 5486, 2016.

[61] L. Cho, E. J. Seo, G. S. Jung, D. W. Suh, and B. C. De Cooman, "Surface Selective Oxidation of Sn-Added CMnSi TRIP Steel," Metall. Mater. Trans. A, vol. 47, no. 4, pp. 1705–1719, 2016.

[62] G. Lyudkovsky, "The Effect of Antimony on Internal Oxidation and Magnetic Properties of Si-Al Electrical Steels," IEEE Trans. Magn., vol. 22, no. 5, pp. 508–510, 1986.

[63] M. De Meyer, D. Vandershueren, and B. C. De Cooman, "The Influence of Substitution of Si by Al on the Properties of Cold Rolled C-Mn-Si TRIP Steels," ISIJ Int., vol. 39, no. 8, pp. 813– 822, 1999. [41]

[64] E. M. Bellhouse and J. R. McDermid, "Selective Oxidation and Reactive Wetting during Galvanizing of a CMnAl TRIP-Assisted Steel," Metall. Mater. Trans. A, vol. 42A, no. 9, pp. 2753– 2768, 2011.

[65] A. E. Nehrenberg, "The Temperature Range of Martensite Formation," Trans. AIME, vol. 167, pp. 494–498, 1946.

[66] H. Farahani, W. Xu, H. Chen, and S. van der Zwaag, "Differences in the predicted phase fractions after intercritical annealing in medium Mn steels using different equilibrium assumptions"," in 2nd HMnS Conference Proceedings, 2014, pp. K1-31.

[67] J. R. McDermid, H. S. Zurob, and Y. Bian, "Stability of Retained Austenite in High-Al, Low-Si TRIP-Assisted Steels Processed via Continuous Galvanizing Heat Treatments," Metall. Mater. Trans. A, vol. 42, no. 12, pp. 3627–3637, 2011.

[68] P. Jacques, Q. Furnémont, A. I. M. Mertens, and F. Delannay, "On the sources of work hardening in multiphase steels assisted by transformation-induced plasticity," Philos. Mag. A, vol. 81, no. 7, pp. 1789–1812, 2001.

[69] A. Perlade, O. Bouaziz, and Q. Furnemont, "A physically based model for TRIP-aided carbon steels behav iour," Mater. Sci. Eng. A, vol. 356A, pp. 145–152, 2003.

[70] G. A. Thomas and J. F. Hansman, "Development, Design, and Industrial Launch of Next- 66 Generation Steel," in International Symposium on New Developments in Advanced HighStrength Sheet Steels, 2017, pp. 11–18.

[71] A. K. Sachdev, "Effect of Retained Austenite on the Yielding and Deformation Behavior of a Dual Phase Steel," Acta Metall., vol. 31, no. 12, pp. 2037–2042, 1983.

[72] K. Sugimoto, T. Iida, J. Sakaguchi, and T. Kashima, "Retained Austenite Characteristics and Tensile Properties in a TRIP Type Bainitic Sheet Steel," ISIJ Int., vol. 40, no. 9, pp. 902–908, 2000.

[73] W. Q. Cao, C. Wang, J. Shi, M. Q. Wang, W. J. Hui, and H. Dong, "Microstructure and mechanical properties of Fe–0.2C–5Mn steel processed by ART-annealing," Mater. Sci. Eng. A, vol. 528, no. 22–23, pp. 6661–6666, Aug. 2011.

[74] S.-J. Lee, S. Lee, and B. C. De Cooman, "Mn partitioning during the intercritical annealing of ultrafine-grained 6% Mn transformation-induced plasticity steel," Scr. Mater., vol. 64, no. 7, pp. 649–652, Apr. 2011.

[75] A. Arlazarov and M. Goune, "Characterization of microstructure formation and mechanical behavior of an advanced medium Mn steel Development of ecological ceramic/polymer nanocomposites for biomedical and energy storage applications View project Spinodal decomposition View project," 2012.

[76] N. Nakada, K. Mizutani, T. Tsuchiyama, and S. Takaki, "Difference in transformation behavior between ferrite and austenite formations in medium manganese steel," in 2nd HMnS Conference Proceedings, 2014, pp. K2-89.

[77] P. J. Gibbs, E. De Moor, M. J. Merwin, B. Clausen, J. G. Speer, and D. K. Matlock, "Austenite stability effects on tensile behavior of manganese-enriched- austenite transformation-induced plasticity steel," Metall. Mater. Trans, vol. 42, no. 12, pp. 3691–3702, 2011.

[78] B. Sun, N. Vanderesse, F. Fazeli, C. Scott, J. Chen, P. Bocher, M. Jahazi, and S. Yue, "Discontinuous strain-induced martensite transformation related to the Portevin-Le Chatelier effect in a medium manganese steel," Scr. Mater., vol. 133, pp. 9–13, 2017.

 J. Mahieu, S. Claessens, and B. C. De Cooman, "Galvanizability of High-Strength Steels for Automotive Applications," Metall. Mater. Trans. A, vol. 32, no. 11, pp. 2905–2908, 2001.

[79] X. G. Wang, L. Wang, and M. X. Huang, "Kinematic and thermal characteristics of Lüders and Portevin-Le Chatelier bands in a medium Mn transformation-induced plasticity steel," Acta Mater., vol. 124, pp. 18–29, 2017.

[80]J. Mahieu, S. Claessens, and B. C. De Cooman, "Galvanizability of High-Strength Steels for Automotive Applications," Metall. Mater. Trans. A, vol. 32, no. 11, pp. 2905–2908, 2001.

A. R. Marder, "The metallurgy of galvanized coatings," Progr. Mater. Sci, vol. 45, pp. 191– 271, 2000.

[80] E. A. Silva, "Private Communication," 2005.

[81] Morris, "FREED Thermodynamic Database v7.8.1." 2013

[82] D. Huin, P. Flauder, and J. B. Leblond, "Numerical Simulation of Internal Oxidation of Steels during Annealing Treatments," Oxid. Met., vol. 64, pp. 131–167, 2005.

[83] R. A. Rapp, "Kinetics, Microstructures and Mechanism of Internal Oxidation - Its Effect and Prevention in High Temperature Alloy Oxidation," Corrosion, vol. 21, no. 12, pp. 382– 402, 1965.

[84] I. G. Wright, R. B. Dooley, "A review of the oxidation behaviour of structural alloys in steam," *International Materials Reviews,* vol. 55, no. 3, pp. 129-167, 2013.

[85] Morris, "FREED Thermodynamic Database v7.8.1." 2013

[86] S. Alibeigi, "Short-Term Formation Kinetics of the Continuous Galvanizing Interfacial Layer on Mn-containing Steels (Doctoral dissertation, PhD thesis)," McMaster University, Hamilton, ON, Canada, 2014.

[87] W.Zhoa, Y. Kang, J.M. A. Orozoco, B. Gleeson, "Quantitative approach for determining the critical volume fraction for the transition from internal to external oxidation," Oxidation of Metals, vol.83, no . 3-4,pp.187-201,2015.

[88] C. Wagner, "Z. fu¨r Elektrochem. Ber. Bunsenges," *Physical Chemistry,* vol. 63, pp. 772-82, 1992.

[89] R. A. Rapp, "Kinetics, microstructures and mechanism of internal oxidation-its effect and prevention in high temperature alloy oxidation," *Corrosion,* vol. 21, no. 12, pp. 382-401, 1965.

[90]] D. Huin, P. Flauder, and J. B. Leblond, "Numerical Simulation of Internal Oxidation of Steels during Annealing Treatments," Oxid. Met., vol. 64, pp. 131–167, 2005.

[91] M. Guttmann, "Diffusive Phase Transformations in Hot-Dip Galvanizing," Mater. Sci. Forum, vol. 155–156, pp. 527–548, 1994.

[92] J. R. McDermid, M. H. Kaye, and W. T. Thompson, "Fe Solubility in the Zn-Rich Corner of the Zn-Al-Fe System for Use in Continuous Galvanizing and Galvannealing," Metall. Mater. Trans. B, vol. 38, no. 2, pp. 215–230, 2007.

[93] L. Chen, R. Fourmentin, and J. R. McDermid, "Morphology and Kinetics of Interfacial Layer Formation during Continuous Hot-Dip Galvanizing and Galvannealing," Metall. Mater. Trans. A, vol. 39A, pp. 2128–2142, 2008.

[94] J. Nakano, "Doctoral Thesis," McMaster University, 2006.

[95] H. Liu, Y. He, and L. Li, "Application of thermodynamics and Wagner model on two problems in continuous hot-dip galvanizing," J. Appl. Surf. Sci., vol. 256, no. 5, pp. 1399– 1403, 2009.

[96] Y. Suzuki, T. Yamashita, Y. Sugimoto, S. Fujita, and S. Yamaguchi, "Thermodynamic Analysis of Selective Oxidation Behavior of Si and Mn-added Steel during Recrystallization Annealing," ISIJ Int., vol. 49, no. 4, pp. 564–573, 2009.

[97] R. Khondker, A. I. M. Mertens, and J. R. McDermid, "Effect of annealing atmosphere on the galvanizing behavior of a dual-phase steel," Mater. Sci. Eng. A, vol. 463, no. 1–2, pp. 157–165, 2007.

[98] E. M. Bellhouse, A. I. M. Mertens, and J. R. McDermid, "Development of the surface structure of TRIP steels prior to hot-dip galvanizing," Mater. Sci. Eng. A, vol. 463, no. 1, pp. 147–156, 2007.

[99] C. E. Jordan and A. R. Marder, "Fe–Zn phase formation in interstitial-free steels hot-dip galvanized at 450 ° C Part II 0.20 wt% Al–Zn baths," J. Mater. Sci., vol. 32, pp. 5603–5610, 1997.

[100] E. M. Bellhouse, "Galvanizing of Al-Si TRIP-Assisted Steels," McMaster University, 2010.

[101] P. Vivek, 2019, 'MICROSTRUCTURAL EVOLUTION AND MECHANICAL PROPERTIES OF MEDIUM MANGANESE TRANSFORMATION INDUCED PLASTICITY THIRD GENERATION ADVANCED HIGH STRENGTH STEEL', MASc thesis, McMaster University, Hamilton, 2019.

[102] ASTM A 653/A 653M – 05, (2005) Standard specification for steel sheet, zinc-coated (galvanized) or zinc-iron alloy-coated (galvannealed) by the hot-dip process.

[103] C. Wagner, Zh. Elektrochem., 63 (1959) 772-782.

[104] G. Seyed Mousavi, J.R. McDermid, 'SELECTIVE OXIDATION AND REACTIVE WETTING OF 2MN-SI STEELS DURING CONTINUOUS HOT-DIP GALVANIZING' Surf. Coat. Technol. 351 (2018) 11-20.

[105] L. Cho, M.S. Kim, Y.H. Kim, B.C. De Cooman, '"Mn partitioning during the intercritical annealing of ultrafine-grained 6% Mn transformation-induced plasticity steel' Metall. Mater. Trans. A 45A (2014) 4484- 4498.

[106] R. Sagl, A. Jarosik, D. Stifter, G. Angeli, Corros, "Tailoring of oxide morphology and crystallinity on advanced high-strength steel surfaces prior hot-dip galvanizing" Sci. 70 (2013) 268-275

[107] J-B. Brunac, D. Huin, J-B. Leblond, "Effect of dew point on the reactive wetting of a C-2Mn-1.3 Si (wt%) advanced high strength steel during continuous galvanizing", Oxid. Met., 73 (2010) 565-589.